On the Rapid Intensification of Hurricane Wilma (2005). Part III: Effects of Latent Heat of Fusion

WILLIAM MILLER, HUA CHEN, AND DA-LIN ZHANG

Department of Atmospheric and Oceanic Science, University of Maryland, College Park, College Park, Maryland

(Manuscript received 21 December 2014, in final form 23 June 2015)

ABSTRACT

The impacts of the latent heat of fusion on the rapid intensification (RI) of Hurricane Wilma (2005) are examined by comparing a 72-h control simulation (CTL) of the storm to a sensitivity simulation in which the latent heat of deposition is reduced by removing fusion heating (NFUS). Results show that, while both storms undergo RI, the intensification rate is substantially reduced in NFUS. At peak intensity, NFUS is weaker than CTL by 30 hPa in minimum central pressure and by 12 $\mathrm{m\,s^{-1}}$ in maximum surface winds. The reduced rate of surface pressure falls in NFUS appears to result hydrostatically from less upper-level warming in the eye. It is shown that CTL generates more inner-core convective bursts (CBs) during RI, with higher altitudes of peak vertical motion in the eyewall, compared to NFUS. The latent heat of fusion contributes positively to sufficient eyewall conditional instability to support CB updrafts. Slantwise soundings taken in CB updraft cores reveal moist adiabatic lapse rates until 200 hPa, where the updraft intensity peaks. These results suggest that CBs may impact hurricane intensification by inducing compensating subsidence of the lower-stratospheric air, and the authors conclude that the development of more CBs inside the upper-level radius of maximum wind and at the higher altitude of latent heating all appear to be favorable for the RI of Wilma.

1. Introduction

There has been considerable interest during recent years in the understanding and prediction of rapid intensification (RI) of tropical cyclones (TCs), which is defined as a 42 $\mathrm{hPa\,day^{-1}}$ drop in minimum central pressure P_{MIN} for western Pacific TCs (Holliday and Thompson 1979) or a 15 $\mathrm{m\,s^{-1}\,day^{-1}}$ maximum surface wind speed (V_{MAX}) increase for Atlantic TCs (Kaplan and DeMaria 2003). Hurricanes Opal (1995), Bret (1999), and Charley (2004) are examples of TCs that underwent unexpected RI episodes within 48 h of making landfall on the U.S. coastline (Lawrence et al. 1998, 2001; Franklin et al. 2006), highlighting the need for improving our understanding of the RI process. Using the Statistical Hurricane Intensity Prediction Scheme (SHIPS) database, Kaplan and DeMaria (2003) identified environmental conditions that are favorable for RI, which include warm sea surface temperatures (SSTs), weak vertical wind shear, stronger easterly winds in the upper troposphere, and high relative humidity in the lower troposphere. Clearly, these environmental conditions are not distinguished from those favoring tropical cyclogenesis and normal TC intensification rates. In addition, we have limited knowledge on the roles of inner-core processes and on any potentially synergistic relationship between inner-core processes and favorable environmental conditions.

Observations have shown deep convective elements with anomalously cold cloud tops erupting near the center of TCs just prior to or during RI (Rodgers et al. 1998, 2000; Price et al. 2009; Guimond et al. 2010; Fierro and Reisner 2011; Stevenson et al. 2014). We will adopt the most commonly used term, convective bursts (CBs), for this study. In their observational study of Hurricane Dennis (2005), Guimond et al. (2010) found 20 $\mathrm{m\,s^{-1}}$ eyewall updrafts at an altitude of 12–14 km, flanked by intense upper-level downdrafts of 10–12 $\mathrm{m\,s^{-1}}$, several hours before the storm commenced a period of RI. Heymsfield et al. (2001) showed CBs overshooting the tropopause by 2 km adjacent to the developing eye of Hurricane Bonnie (1998), and later, shortly before the storm reached maximum intensity, they found deep

---

Corresponding author address: Dr. Da-Lin Zhang, Dept. of Atmospheric and Oceanic Science, University of Maryland, College Park, 2419 CSS Building, College Park, MD 20742-2425.
E-mail: dalin@atmos.umd.edu

DOI: 10.1175/JAS-D-14-0386.1

mesoscale subsidence extending from $z = 15$ km at cloud top downward and radially inward along the eye–eyewall interface. They hypothesized that this downdraft, originating as compensating subsidence of stratospheric air and being maintained by evaporative and sublimative cooling of hydrometeors detrained from the eyewall, may have contributed up to 3°C of warming aloft in the eye.

Hurricane Wilma (2005) underwent an 18-h RI period with a record-breaking deepening rate of 83 hPa $(12\,\mathrm{h})^{-1}$, which culminated in the storm becoming the strongest hurricane ever recorded in the Atlantic basin, featuring a minimum central pressure of 882 hPa and maximum surface winds exceeding 80 m s^{-1}. In Chen et al. (2011, hereafter Part I), the intensity and structural changes of Hurricane Wilma prior to, during, and after RI have been successfully reproduced with a 72-h (0000 UTC 18 October–0000 UTC 21 October 2005) prediction using the Weather Research and Forecasting (WRF) Model with a quadruply nested (27, 9, 3, and 1 km) grid and initial and lateral boundary conditions that are identical to the Geophysical Fluid Dynamics Laboratory's then-operational data. Then, Zhang and Chen (2012, hereafter ZC12) used the hydrostatic equation to demonstrate how the warming above the 380-K isentrope in Wilma's eye, which results primarily from the descent of stratospheric air, is responsible for the largest portion of the surface pressure falls during RI. In Chen and Zhang (2013, hereafter Part II), the collective action of a series of CBs straddling the radius of maximum wind (RMW) was shown to contribute to the warm-core development through the cyclonic propagation of subsidence-induced warm anomalies into the region aloft in the eye. This result was consistent with the work of Hack and Schubert (1986) and Vigh and Schubert (2009), who showed that latent heat release (LHR) inside the RMW, where inertial stability is large, is more efficient for TC intensification than LHR in the outer regions. Observations have also shown LHR inside the RMW to be a key characteristic of rapidly intensifying TCs (Rogers et al. 2013; Stevenson et al. 2014; Rogers et al. 2015). Recently, Ohno and Satoh (2015) simulated an upper-level warm core, in an intensifying idealized TC, that developed as a result of stratospheric subsidence generated by a secondary circulation that was forced by diabatic heating in the eyewall. They found that the upward penetration of the cyclonic vortex into the high static stability region above the tropopause was a key factor in the generation of the forced secondary circulation at these altitudes, because the enhanced inertial stability caused an increase in the local Rossby depth.

Given the substantial evidence showing that CBs and their compensating subsidence positively affect the RI of TCs, we are motivated to examine the impact of upper-level LHR associated with ice microphysical processes on the generation of CBs. For this study, we hypothesize that LHR from deposition (vapor to ice) processes in the upper portion of the eyewall helps account for the development of CBs and that its occurrence within the RMW is the key to the RI of TCs. Although there is ample evidence showing the reinvigoration of tropical oceanic updrafts at higher levels associated with ice LHR processes (Zipser 2003; Zhu and Zhang 2006; Romps and Kuang 2010; Fierro et al. 2012), few quantitative studies have been performed to examine how upper-level LHR inside the RMW is related to TC intensification. The effects of ice LHR processes on the RI of TCs have also been speculated (Guimond et al. 2010; Molinari and Vollaro 2010).

Thus, the objectives of this study are to (i) investigate the impact of upper-level depositional LHR on changes to TC structure and intensity through the generation of eyewall CBs and (ii) examine the thermodynamic and ice microphysical structures of CBs in the eyewall. The above objectives will be achieved by comparing the Hurricane Wilma prediction described in Part I, ZC12, and Part II, referred to herein as the control (CTL), to a sensitivity simulation (NFUS) in which the latent heat of deposition is reduced, while all the other model parameters are kept identical, and then studying differences in intensity and structures. Through this study, we wish to answer the following questions: To what extent does the LHR from deposition determine the intensity and coverage of CBs, and what impact does this have on the RI of Hurricane Wilma? How will it affect the amplitude and altitude of the upper-level warm core? How will the vertical motion in the eyewall, eye, and rainband regions respond to the LHR from deposition?

The next section describes the WRF microphysics scheme and experimental design used to perform the NFUS experiment. Section 3 compares Wilma's intensity and structural changes between the CTL and NFUS simulations. Section 4 discusses CB statistics. Section 5 analyzes the eyewall, eye, and rainband vertical motion profiles. A heat budget analysis used for understanding the subsidence warming in the eye is also presented. Section 6 examines the thermodynamic and ice microphysical structures of CBs in the eyewall. A summary and concluding remarks are given in the final section.

2. Experiment design

The 72-h WRF Model predictions use the Thompson et al. (2004, 2008) cloud microphysics scheme, which contains six classes of water substance (i.e., water vapor, cloud water, rain, snow, graupel, and cloud ice); see

Part I for a detailed description of the model initialization and other physics options used. Unlike many bulk schemes, which use exponential distributions for hydrometeor size, the Thompson scheme utilizes gamma distributions with tunable intercept parameters. As an example of this added complexity, the graupel size distribution depends on the mass mixing ratio such that in regions with high mixing ratios, such as deep convective updraft cores, the graupel distributions shift toward larger sizes, thus increasing the mass-weighted mean fall speeds to more physically realistic values. In the Thompson scheme, depositional heating results from the deposition of vapor onto cloud ice, snow, and graupel, as well as from ice nucleation, while freezing heating is associated with liquid-to-ice processes, which include the homogeneous and heterogeneous freezing of water droplets, as well as the riming of graupel and snow.

Our rationale for focusing on depositional heating impacts is based on the high altitude of this heat source and on the magnitude of the LHR. A parcel-following modeling study using the Lin–Farley–Orville microphysics scheme showed LHR from deposition to peak several kilometers higher than freezing heating in tropical oceanic cumulonimbus (Fierro et al. 2012). The authors attributed this phenomenon to more efficient warm-rain processes and lower cloud condensation nuclei (CCN) concentrations (relative to continental storms) causing rapid depletion of cloud water above the freezing level and limiting freezing heating to a shallow layer. These results were consistent with observations of radar reflectivity and cloud water concentrations decreasing more rapidly with height for TCs in comparison to land-based storms (Jorgensen et al. 1985, hereafter JZL). The strong dependence of CB activity on warm SSTs (Part II) suggests that a high–equivalent potential temperature (θ_e) maritime boundary layer (MBL) environment could be a critical precondition for initiating updrafts strong enough to tap into depositional heating sources aloft. A significant buoyant acceleration boost should result from the much greater magnitude of the latent heat of deposition L_d (2838 J g^{-1}) compared to the latent heat of fusion L_f (289 J g^{-1}; Rogers and Yau 1989); the difference between the two is the latent heat of vaporization L_v: $L_d = L_v + L_f$. To study the impacts of LHR from deposition, the NFUS sensitivity simulation uses a modified microphysics scheme whereby the fusion component of depositional heating is removed so that $L_d = L_v$. No other aspects of the microphysics code are altered.

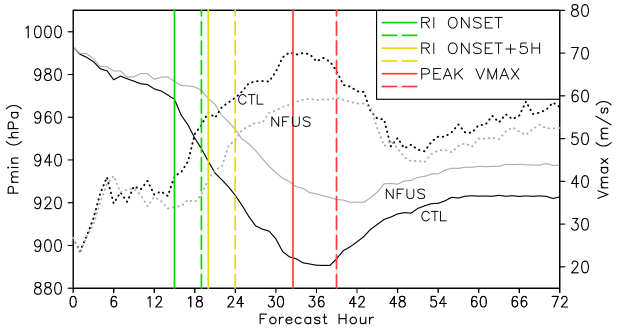

FIG. 1. Time series of P_{MIN} (solid) and V_{MAX} (dotted) for CTL (black) and NFUS (gray) from the 3-km-resolution domain. Vertical lines denote characteristic times discussed in the text (solid for CTL and dashed for NFUS).

3. Intensity changes

Figure 1 compares the time series of P_{MIN} and V_{MAX} (at $z = 10$ m) between CTL and NFUS. Following an initial 15-h spinup, CTL commences a period of rapid deepening in P_{MIN} and strengthening in V_{MAX}. By 32 h into the integration, here called 32:00, V_{MAX} levels off near 72 m s^{-1}, while P_{MIN} continues to fall, albeit less rapidly, until it reaches a minimum of 890 hPa[1] around 36:00. Although seemingly inconsistent with the conventional pressure–wind relationship, the slower rate of V_{MAX} increase during the latter part of the rapid deepening phase has been attributed to intense frictional effects in Wilma's exceptionally small eyewall and to the lack of any further contraction (Part I; Kieu et al. 2010). This 21-h (i.e., 15:00–36:00) period is characterized by a P_{MIN} drop of 78 hPa and a V_{MAX} increase of 27 m s^{-1}, easily exceeding the conventional RI threshold, and we will refer to it as the CTL RI phase for the remainder of this study. After 36:00, a developing outer eyewall begins cutting off the supply of high-θ_e air to the inner-core region, weakening the storm and beginning an eyewall replacement cycle (ERC). Beyond 54:00, as the outer eyewall begins to contract, P_{MIN} reaches a steady state, while V_{MAX} gradually increases.

Removal of the fusion component of depositional heating results in a significantly weaker storm at the time of peak intensity, with a 30-hPa increase in P_{MIN} (920 hPa in NFUS vs 890 hPa in CTL) and a 12 m s^{-1} drop in V_{MAX} (60 m s^{-1} in NFUS vs 72 m s^{-1} in CTL). At 19:00, a sustained period of rapid P_{MIN} falls begins, lasting through 35:00, at which time P_{MIN} begins falling at a rate of 0.9 hPa h^{-1} until it reaches a minimum at 42:00. Despite showing a reduced intensification rate, the NFUS 19:00–35:00 period still qualifies as RI per the conventional definition, with an average deepening rate

---

[1] Slight differences in peak intensity and intensification rate from those reported in Part I (890 vs 889 hPa and 6 vs 7 hPa h^{-1}), as well as small differences in other fields, likely result from use of different WRF data postprocessing packages.

of 3.0 hPa h^{-1}. After reaching peak intensity, NFUS also undergoes an ERC and weakens before gradually reintensifying with the contraction of the new eyewall. The intensity differences become less pronounced following the ERC, and the simulation ends with NFUS 15 hPa weaker than CTL. The model-predicted tracks for the two simulations (not shown) do not diverge until the last few hours of RI, and even thereafter, both storm tracks remain over the same SSTs at any given hour. Therefore, the intensity differences presented in Fig. 1 should not result from environmental influences.

In summary, the NFUS storm undergoes the same basic structural changes observed in CTL. While NFUS still undergoes RI, the onset is 4 h later, the duration is 5 h shorter, and the average deepening rate over the RI period is lower (viz., 3.0 hPa h^{-1} for 19:00–35:00 vs 3.7 hPa h^{-1} for 15:00–36:00 in CTL). The peak hourly deepening rate is slightly reduced (5 vs 6 hPa h^{-1} in CTL). The remainder of this study will focus primarily on the RI period.

To see how the RI in P_{MIN} differs between the two simulations, Fig. 2 compares their time–height cross sections of perturbation temperatures $T'(z, t)$, along with potential temperature θ, taken at the eye center. For both simulations, the 370-K θ surface begins to descend at RI onset (15:00 in CTL and 19:00 in NFUS), indicating a period of increased upper-level warming. Between 33:00 and 58:00, NFUS develops a 12°–14°C warm anomaly, which is still significant but far less substantial than the peak warming of over 20°C that CTL shows at 36:00. During the course of RI, the NFUS isentropic surfaces fail to descend as far, with the $\theta = 370$-K contour lowering to $z = 9$ km and $z = 11$ km in CTL and NFUS, respectively, and with the $\theta = 390$-K contour never dipping below $z = 16$ km in NFUS, despite the fact that it reaches $z = 14$ km at 36:00 in CTL. Throughout the RI period, the warm core remains in the upper troposphere, near $z = 14$ km in CTL and roughly 1 km lower in NFUS. It appears likely, based on the hydrostatic arguments of ZC12, that the weaker NFUS upper-level warming accounts for a large portion of the 30-hPa reduction in peak storm intensity.

Since Part II attributed the CTL-simulated intense upper-level warm core to the development of CBs, in Fig. 3 we compare the distribution of CB elements relative to the lower- and upper-level RMWs, together with radar reflectivity at $z = 1$ km, taken at a few time steps. The CB elements are counted[2] by the same procedure as that used by Part II (i.e., vertical grid columns are identified that contain at least one point with $w \geq 15$ m s^{-1} for $z \geq 11$ km). For both simulations, the RI period is characterized by a contracting and increasingly coherent eyewall, evident in both the radar reflectivity trends and in the tendency for the local $z =$ 1- and 11-km RMWs to follow an increasingly circular pattern about the storm center (Figs. 3a–c for CTL and Figs. 3e–g for NFUS). Similarly, the Rogers (2010) Hurricane Dennis simulation showed increasingly organized convection surrounding the eye during RI. During this period, CB activity remains concentrated near and inside the $z = 11$-km RMW, where the inertial stability and the efficiency of LHR for TC intensification are high (Hack and Schubert 1986). This is especially apparent once the upper-level tangential wind profiles become more symmetric in CTL (Fig. 3b) and in NFUS (Fig. 3f). By 39:00 in CTL and 45:00 in NFUS, both storms are in the midst of an ERC (Figs. 3d,h), as shown by the collapse of inner-eyewall convection with the development of an outer eyewall near the 60-km radius. For CTL, CB elements now cluster in the outer eyewall, whereas previously they had remained near the $z = 1$-km RMW, where low-level θ_e and convergence had been maximized.

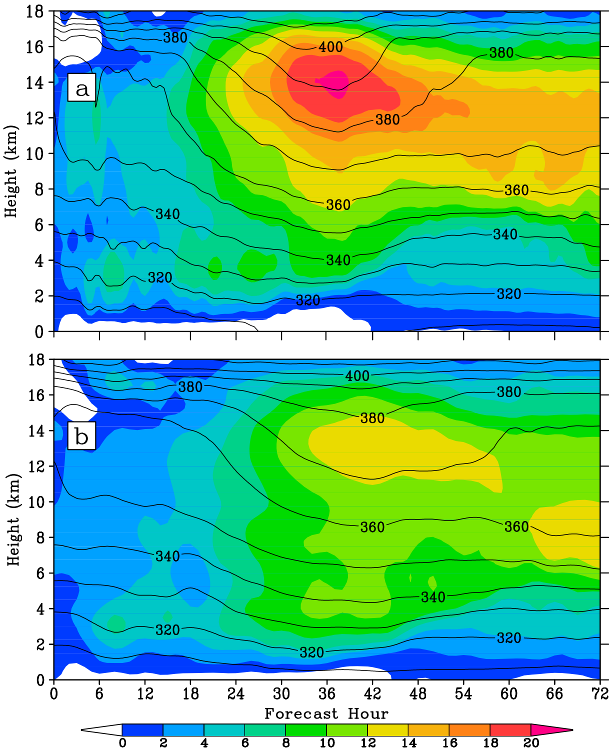

FIG. 2. Time series of $T'(z, t)$ [shaded; K; calculated with respect to 1000 km × 1000 km area-averaged $\overline{T(z)}$ at initial time] and potential temperature (contours; K) at storm center for (a) CTL and (b) NFUS from the 3-km-resolution domain.

---

[2] Note that Part II counted CB elements from three time levels at 5-min intervals, whereas they are counted herein only from one time level, thus causing fewer CB elements to be seen at $t = 15{:}00$ (cf. Fig. 3a herein and Fig. 3d in Part II).

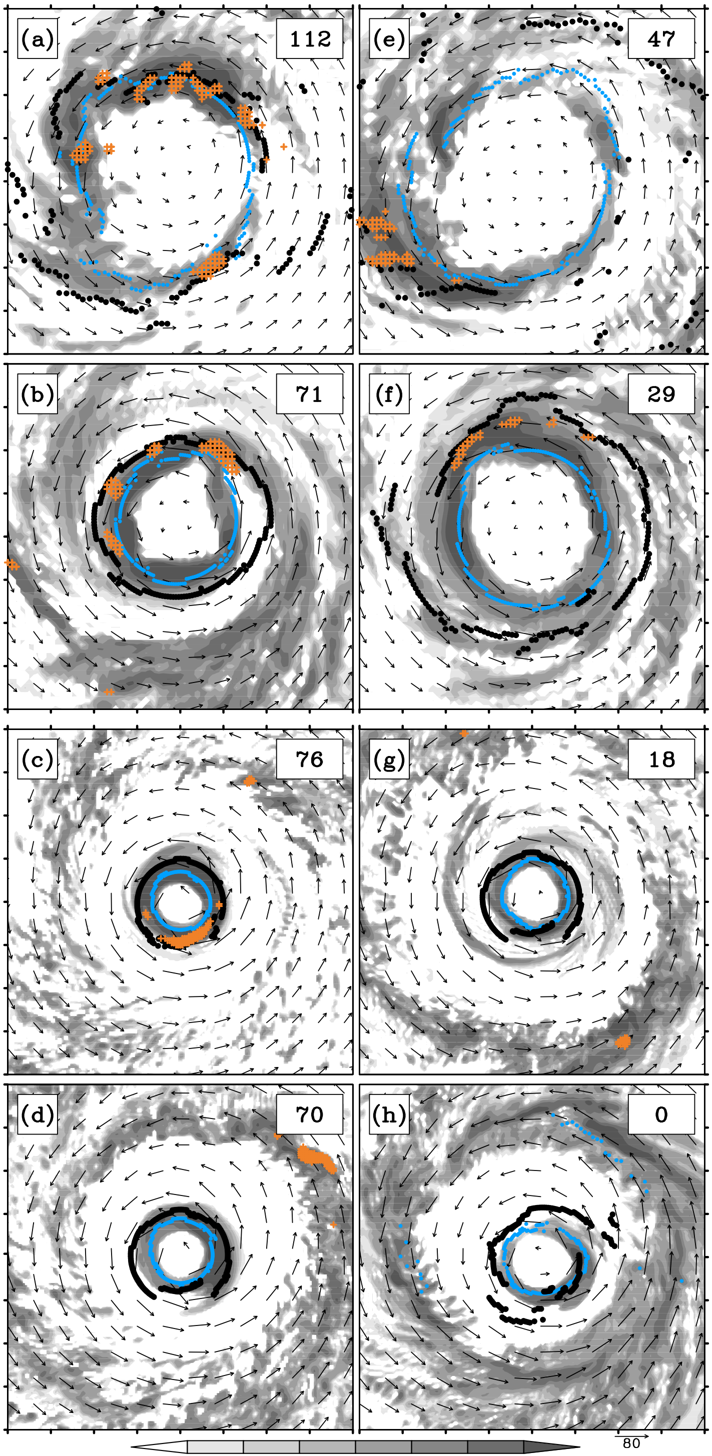

FIG. 3. Radar reflectivity (shaded; dBZ) and storm-relative-flow vectors (m s^{-1}) at z = 1-km level with CB elements (orange crosses) and azimuthally dependent z = 1-km (blue dots) and 11-km (black dots) RMW. (left) CTL at (a) 15:00, (b) 20:00, (c) 32:30, and (d) 39:00. (right) NFUS at (e) 19:00, (f) 24:00, (g) 39:00, and (h) 45:00. For (a),(b),(e), and (f), an 80 km × 80 km subdomain is used (scale ticks mark 10-km intervals), while for (c),(d),(g), and (h), a 160 km × 160 km subdomain is used (scale ticks mark 20-km intervals). Upper-right label boxes display total number of CB elements in the subdomain. Data for Fig. 3 and all subsequent figures are taken from the 1-km-resolution domain.

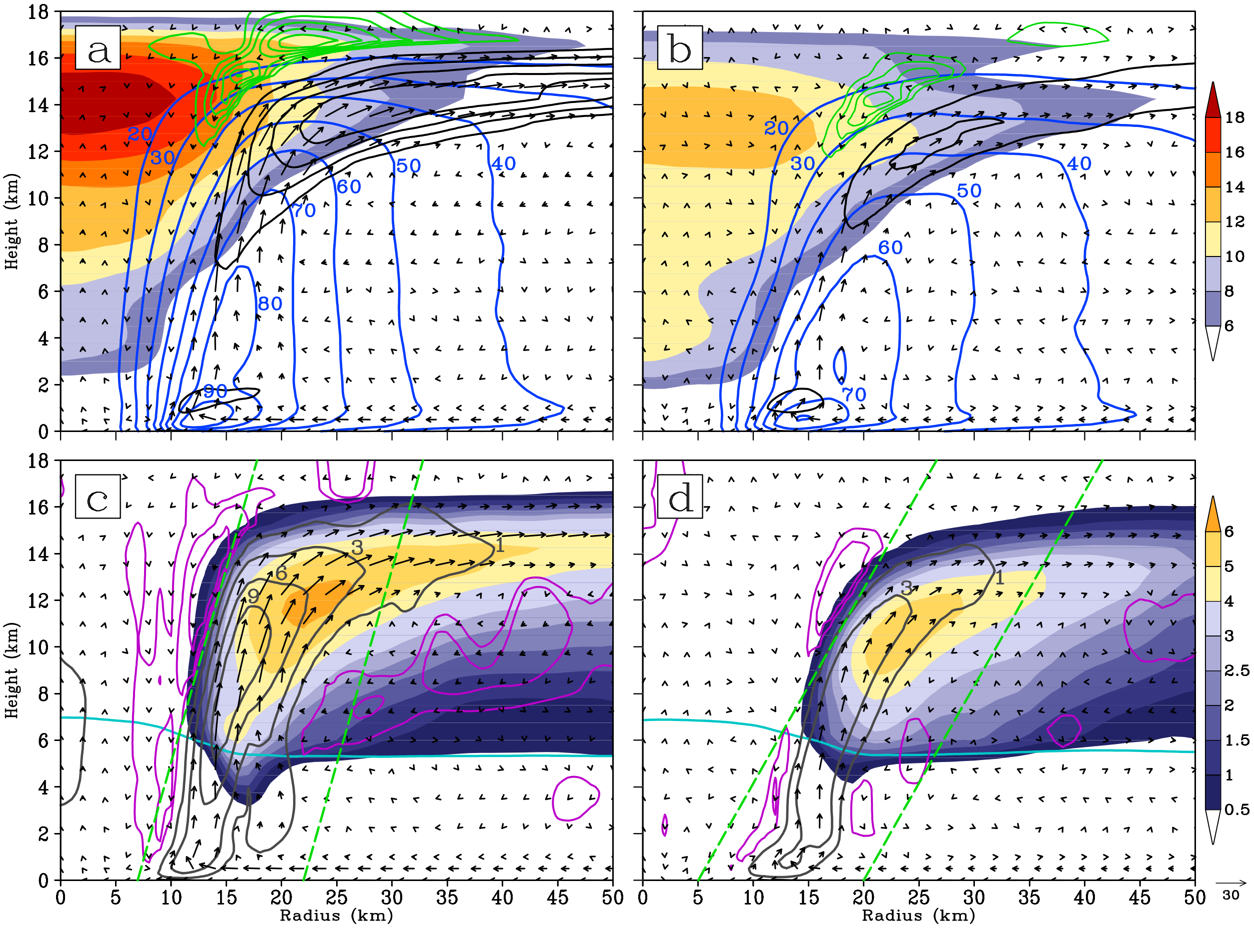

FIG. 4. Azimuthally averaged structures for (left) CTL at 32:30 and (right) NFUS at 39:00. (a),(b) $T'(z, t)$ (shaded; K) with tangential winds (blue contours; $\mathrm{m\,s^{-1}}$), radial outflows (black contours; every $5\,\mathrm{m\,s^{-1}}$), and upper-level radial inflows (green contours; every $0.5\,\mathrm{m\,s^{-1}}$). (c),(d) Total frozen hydrometeors (shaded; $\mathrm{g\,kg^{-1}}$) with vertical motion (upward, gray contours: 1, 3, 6, and $9\,\mathrm{m\,s^{-1}}$; downward, purple contours: -1.0, -0.5, and $-0.25\,\mathrm{m\,s^{-1}}$) and with the freezing level marked in light blue. For in-plane flow vectors ($\mathrm{m\,s^{-1}}$) in all panels, vertical motions are multiplied by 3. Green dashed lines in (c) and (d) show radial boundaries of the slanted eyewall defined in section 5 at those times.

The following section will present a more detailed analysis of CB activity and its impact on the RI of both storms.

Figure 4 compares azimuthally averaged structures at the time of peak V_{MAX} (32:30 in CTL and 39:00 in NFUS). Before discussing the differences, note that both CTL and NFUS display the classic "in–up–out" secondary circulation of a mature TC, with a low-level inflow peaking just outside the RMW, a sloped updraft core, and an upper-level main outflow branch in the z = 10–16-km layer (Figs. 4a,b). Like CTL, NFUS shows two features identified in ZC12 and Part II that facilitate upper-level warm-core development. First, the upper-level outflow layer coincides with the height of the warm core, helping protect the warmer air inside the RMW from ventilation by environmental flows. Second, both generate an upper-level return inflow branch that extends downward from above the main outflow into the eye region near the altitude of peak warming (Figs. 4a,b). Possibly driven by the mass sink and upper-level convergence above the eye and maintained by evaporative/sublimative cooling from detrained eyewall hydrometeors, the return inflow may contribute to warm-core development by drawing down stratospheric air (ZC12), although further studies are needed.

Despite these similarities, CTL shows a deeper and more intense primary circulation, as well as a stronger secondary circulation. Comparing the tangential wind fields, CTL and NFUS peak above 90 and $80\,\mathrm{m\,s^{-1}}$, respectively, around z = 1 km, with $60\,\mathrm{m\,s^{-1}}$ winds extending as high as z = 12 km in CTL but only to z = 7.5 km in NFUS (Figs. 4a,b). For CTL, the peak low-level inflow is $5\,\mathrm{m\,s^{-1}}$ stronger (30 vs $25\,\mathrm{m\,s^{-1}}$; not shown) with a deeper inflow depth, while the upper-level outflow branch is 2–4 times more intense (Figs. 4a,b). Figures 4c and 4d compare the azimuthally averaged vertical motion with total frozen hydrometeors, defined here as the integrated cloud ice, snow, and graupel mixing ratios. The CTL updraft core (Fig. 4c) is significantly stronger, with w exceeding $9\,\mathrm{m\,s^{-1}}$ between $z = 6$ and 12 km. NFUS, by comparison, shows peak updrafts of 3–$6\,\mathrm{m\,s^{-1}}$ extending through the depth of the eyewall (Fig. 4d). For both CTL and NFUS, total frozen hydrometeors peak just outside the upper portion of the updraft core. This results from the fact that cloud ice initiates in the updraft region and then grows by deposition to snow while being advected outward by the main outflow (not shown). The peak frozen hydrometeor mixing ratio in CTL is $1\,\mathrm{g\,kg^{-1}}$ greater in magnitude and located 1 km higher. Any difference in the cloud species fields must result from differences in the flow fields as a response to differences in LHR, since the microphysical mass transfer processes in CTL and NFUS are kept identical.

4. Convective burst statistics

Part II showed how CB-induced compensating subsidence could significantly contribute to the development of an upper-level warm core after an upper-level cyclonic circulation develops around the time of RI onset. Meanwhile, a reduction in static stability within the core of the warm anomaly, resulting from the downward displacement of upper-level isentropes, lowers the energy dispersion of internal gravity waves. Nevertheless, the modest CB-induced warming in the eye during the pre-RI stage allows for the development of the upper-level cyclonic flows as a result of local thermal wind balance. Based on these findings, and on the thermal efficiency arguments of Hack and Schubert (1986), we choose to focus herein on CB activity inside the azimuthally averaged $z = 11$-km RMW.

The time series in Fig. 5 show the number of CB elements, counted inside the $z = 11$-km RMW, along with the mean CB radius and $z = 1$- and 11-km RMWs. The CTL CB activity reaches a peak in the first few hours, attributed by Part II to high CAPE in the bogus vortex at time $t = 0$ h, followed by a sharp decline until RI onset, after which time it remains at a stable level throughout the rest of the RI period (Fig. 5a). After the RI period ends at 36:00, inner-core CB activity all but disappears, which is consistent with observational findings of other storms (Molinari et al. 1999). Note that the large cluster of 70 CB elements at 39:00, shown in Fig. 3d, is not counted here because the mean $z = 11$-km RMW has not yet jumped to the outer eyewall. The NFUS simulation (Fig. 5b) shows a similar overall trend, but with significantly reduced CB activity throughout the pre-RI and RI periods. It follows that by removing the fusion component of depositional heating, CB activity inside the $z = 11$-km RMW becomes less prevalent both prior to and during RI, coinciding with a weaker, more slowly developing upper-level warm core and a more modest rate of surface pressure falls. NFUS also shows a similar reduction in CBs within a 100-km radius from the storm center (not shown).

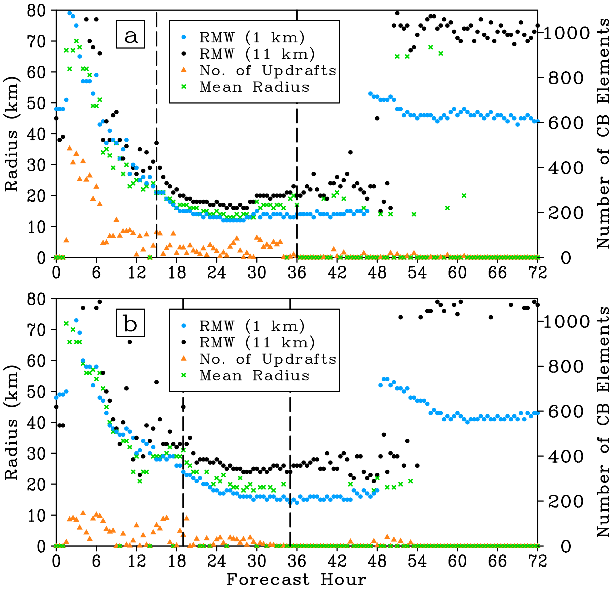

FIG. 5. Time series showing number of CB elements (orange triangles) counted within the $z = 11$-km mean RMW with average radius of counted CB elements (green crosses) for (a) CTL and (b) NFUS. Mean $z = 1$- and 11-km RMWs are shown as blue and black dots, respectively. Dashed vertical lines mark the beginning and end of the RI period.

Figure 6 compares histograms of maximum vertical motion altitude for grid columns with $w \geq 15\,\mathrm{m\,s^{-1}}$, at any height, for the pre-RI, RI, and post-RI periods. During pre-RI, the majority of intense CTL updrafts peak in the upper troposphere, with the largest number peaking at $z = 14$ km. Then, during RI, the favored peak updraft height lowers to $z = 9$ km, with a secondary maximum appearing at $z = 6$ km near the freezing level, although a substantial number of updrafts still peak above $z = 10$ km. During the post-RI phase, a very small number of updrafts reach $15\,\mathrm{m\,s^{-1}}$ and peak near the freezing level. NFUS shows fewer $w \geq 15\,\mathrm{m\,s^{-1}}$ updrafts during the pre-RI and RI phases, with the differences most pronounced in the upper troposphere. For pre-RI, the strong sharp peak at $z = 14$ km is no longer present, replaced by a broader, weaker peak spanning the 9–14-km range. Note the greater-than-threefold reduction in number of occurrences at $z = 14$ km relative to CTL. During RI, NFUS shows similar numbers of intense updrafts at the favored $z = 6$- and 9-km levels, but, for

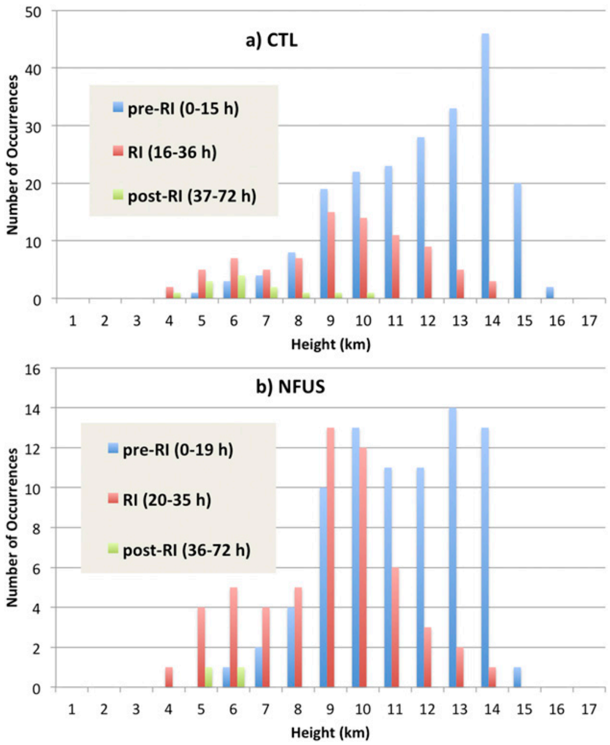

FIG. 6. Histogram of the average number of updraft columns inside the $z = 11$-km mean RMW with $w \geq 15\,\mathrm{m\,s^{-1}}$ for (a) CTL and (b) NFUS, binned by altitude of maximum vertical motion.

heights above $z = 10\,\mathrm{km}$, the NFUS intense updraft count is reduced from CTL by at least one-half. The lower frequency of intense NFUS updrafts peaking above $z = 10\,\mathrm{km}$ during the pre-RI and RI stages suggests that 1) depositional heating plays a crucial role in maintaining intense updrafts at these levels and 2) these updrafts may be important to the development of an upper-level warm core in a rapidly intensifying TC (cf. Figs. 2a,b). Although observational studies have shown that not all CBs induce subsidence flowing into the eye region (Heymsfield et al. 2001), we hypothesize that reduced NFUS CB activity during the RI period results in an overall weaker contribution of subsidence-induced warming toward warm-core development.

Since CB development requires the presence of sufficient conditional instability, Fig. 7a plots azimuthally averaged slantwise convective available potential energy (SCAPE; see the appendix) in CTL over the RI period. Using this method, parcel buoyancy is calculated along slantwise trajectories following constant absolute angular momentum (AAM) surfaces, in contrast to conventional CAPE, where parcel trajectories are vertical. Over the eye region, the steep slope of the AAM surfaces (not shown) makes SCAPE effectively equal to CAPE, and we see a rapid reduction in SCAPE coincident with the marked upper-level warming following RI onset, a result similar to that shown for Super Typhoon (STY) Megi (Wang and Wang 2014). Although the eyewall shows negligible CAPE (not shown), eyewall SCAPE remains greater than $400\,\mathrm{J\,kg^{-1}}$ during RI, which is sufficient to sustain peak updrafts at the level of neutral buoyancy (LNB) $w_{\max}$ of about $30\,\mathrm{m\,s^{-1}}$ (see Fig. 6 in Part II) using the approximation

$$w_{\max} = \sqrt{2\mathrm{SCAPE}},$$

assuming an undiluted ascent in the updraft core. After 18:00, the reservoir of the highest SCAPE shifts from the inner edge to the outer edge of the eyewall, a result supporting the findings of Frisius and Schönemann (2012) that SCAPE outside a TC eyewall could cause superintensity.

The NFUS eyewall (Fig. 7b) shows reduced SCAPE, although the $200\,\mathrm{J\,kg^{-1}}$ available throughout the RI period is still sufficient to generate $20\,\mathrm{m\,s^{-1}}$ updrafts. When calculating NFUS lifted parcel temperatures, ice heating is not permitted, whereas for CTL, the ice adiabat is followed above the freezing level. Despite the fact that the microphysical assumptions used in the SCAPE calculations lack the complexity of the Thompson microphysics scheme (and suppress NFUS freezing heating, which is allowed in the NFUS WRF code), they show that parcel warming from ice LHR is an important contributor to SCAPE in Wilma's eyewall, especially given the increasingly warm environmental temperatures experienced by CTL parcels rising along constant AAM surfaces after RI onset (not shown).

5. Vertical motion profiles and subsidence warming in the eye

We now compare the CTL and NFUS vertical motion profiles, with more focus on how depositional heating affects the full range of updraft intensities, for the eyewall, eye, and outer rainbands. This is done by utilizing cumulative contoured frequency by altitude diagrams (CCFADs; Yuter and Houze 1995b), which show, for a given height, the percentage of horizontal grid points with vertical motion weaker than the abscissa scaled value. The inner and outer eyewall radial boundaries are assigned based on the azimuthally averaged w field such that 1) the $1\,\mathrm{m\,s^{-1}}$ contour at $z = 8\,\mathrm{km}$ and 2) the $3\,\mathrm{m\,s^{-1}}$ contour at all heights are fully enclosed, keeping the CTL and NFUS widths the same for each comparison time. A $6\,\mathrm{km} \times 6\,\mathrm{km}$ box centered on the P_{MIN} centroid defines the eye. The "outer rainbands," by our definition, include all points from 20 km outside the $z = 11$-km RMW to the edge of a

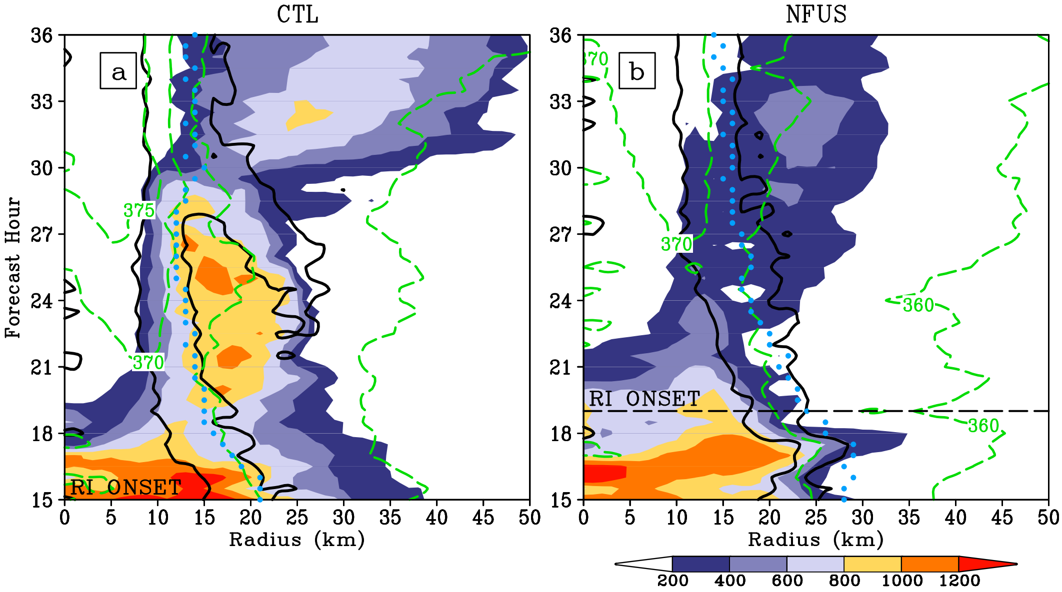

FIG. 7. Azimuthally averaged SCAPE (shaded; J kg^{-1}) with θ_e at parcel lifting level (green dashed contours; K), eyewall boundaries (black solid contours, enclosing areas of $w > 0.5$ m s^{-1} at lifting level), and mean z = 1-km RMW (blue dots) for (a) CTL and (b) NFUS.

200 km × 200 km box surrounding the storm center. All vertical-motion data (see Figs. 8, 9, and 11) are composited from a 5-h time window at 30-min intervals, centered at the indicated time.

a. *Eyewall*

Figure 8 shows CCFADs (Figs. 8a,c) and area-averaged updraft [$\overline{w_{\rm up}(z)}$] and downdraft [$\overline{w_{\rm down}(z)}$] profiles (Figs 8b,d) for the eyewall at two selected times. CTL shows an increased broadening of the updraft distribution with height at 5 h after RI onset (20:00 in CTL and 24:00 in NFUS), with the 95th percentile peaking at 14 m s^{-1} near z = 10 km, and with the 99.9th percentile peaking even higher, at 26 m s^{-1} near z = 13 km (Fig. 8a). Although Black et al. (1996) and Marks and Houze (1987) reported substantially weaker hurricane eyewall updrafts derived from airborne Doppler radar, both studies found that vertical motion peaked in the upper troposphere. However, given our focus on an RI storm and the possibility that the aircraft penetrations may have missed the most intense eyewall updrafts, either by chance or for safety reasons, direct comparison with these studies is rather difficult. Stronger vertical motion may be a characteristic of RI TCs, as the Hurricane Emily eyewall contained peak updrafts and downdrafts of 24 and 19 m s^{-1}, respectively, with mean updrafts and downdrafts roughly twice the strength of those found in other TCs (Black et al. 1994).

The NFUS CCFAD (Fig. 8a) has a similar shape, but significant differences appear in the highest altitudes for the most intense updrafts: at z = 14 km, for example, the strongest 1% of updrafts exceed 7 and 16 m s^{-1} for NFUS and CTL, respectively. Consistent with the moderate-strength portion of the CCFAD updraft distributions (70th percentiles and below), the $\overline{w_{\rm up}(z)}$ profiles (Fig. 8b) show smaller differences. Figure 8b also compares the areal fraction of core elements, defined here as grid points with $|w| \geq 1$ m s^{-1}, following the convention of JZL but without imposing any spatial continuity requirements. Above z = 8 km, the CTL updraft-core areal fraction sharply increases toward a maximum of 70% near z = 12 km. The NFUS updraft-core areal fraction peaks 1 km lower, and between z = 14 and 16 km, it falls to 15%–20% less than CTL. Together, the CCFAD, $\overline{w_{\rm up}(z)}$, and core element fraction profiles provide further evidence of updraft enhancement by depositional LHR at the upper levels during the early stages of RI, with the strongest impacts on the most intense 1% of updrafts above z = 10 km. Rogers et al. (2013) showed a CCFAD comparing eyewall vertical velocities in two composite samples constructed from airborne radar data: one for intensifying ($\Delta V_{\rm MAX} \geq$ 10 m s^{-1} day^{-1}) and the other for steady state hurricanes (see their Fig. 12). They reported little difference in the moderate-strength updrafts, but they did find significantly stronger 99th percentile updrafts above z = 5 km for the intensifying database. Even though NFUS would still have qualified as an "intensifying" storm under their metric, their results suggest that ice process LHR may positively impact the intensification of other TCs.

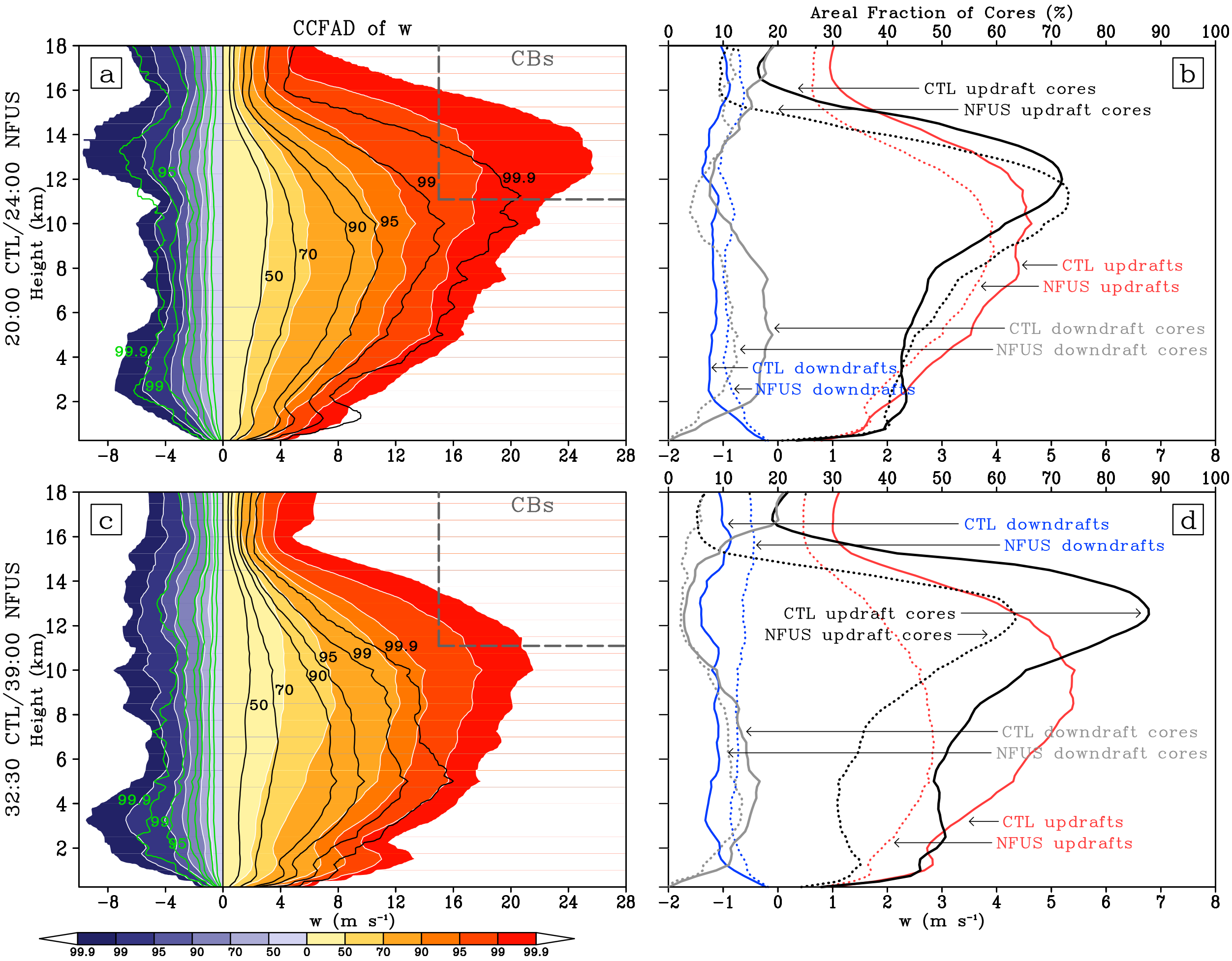

FIG. 8. (a),(c) CCFAD of vertical motion for the eyewall, showing the percentage of grid points in the horizontal plane with w weaker than the abscissa-marked scale value. Updrafts are shaded in orange for CTL and contoured in black for NFUS. Downdrafts are shaded in blue for CTL and contoured in green for NFUS, following the same percentage intervals but with only the outer three lines labeled. (b),(d) Eyewall area-averaged upward ($w > 0\,\mathrm{m\,s^{-1}}$; red) and downward ($w < 0\,\mathrm{m\,s^{-1}}$; blue) vertical-motion profiles with areal fraction of updraft core elements ($w \geq 1\,\mathrm{m\,s^{-1}}$; black) and downdraft core elements ($w \leq -1\,\mathrm{m\,s^{-1}}$; gray) for CTL (solid) and NFUS (dotted). All curves in (b) and (d) show data averaged over a 5-h period centered on the indicated time. (top) At 20:00 in CTL and 24:00 in NFUS and (bottom) at 32:30 in CTL and 39:00 in NFUS.

At the time of the highest V_{MAX} (32:30 in CTL and 39:00 in NFUS), the altitude at which the strongest CTL updrafts peak shifts lower, to near $z = 10\,\mathrm{km}$ (Fig. 8c). Wang and Wang (2014) and McFarquhar et al. (2012) showed a similar lowering of the strongest updrafts' peak height during RI for STY Megi and Hurricane Dennis, respectively, with the former attributing it to increased eyewall tilt and stabilization from upper-level warming and the latter attributing it to increased hydrometeor loading. Both the upper-level warming and increased graupel loading may similarly contribute to the weakening of Wilma's tallest updrafts, as azimuthally averaged $T'(z, t)$ across the CTL updraft core above $z = 11\,\mathrm{km}$ increases by 2°C and peak midlevel-updraft graupel mixing ratios are doubled from 20:00 (not shown). Nevertheless, intense updrafts satisfying our CB criterion remain embedded in the eyewall (cf. Figs. 3c, 5a, and 8c).

The NFUS CCFAD (Fig. 8c) now shows greater differences. For the 90th updraft velocity percentile and above, the peak shifts considerably lower, to $z = 5\,\mathrm{km}$; the narrowing of the updraft CCFAD, relative to CTL, now extends into the midtroposphere, and CB elements are no longer present. A more thermodynamically unfavorable upper-level environment, even compared to CTL, might account for the greater weakening of the 99th percentile NFUS updrafts by peak intensity. Despite its weaker amplitude over the eye, the NFUS upper-level warming has a larger radial extent such that, unlike for CTL, the entire NFUS updraft core between

$z = 7$ and 11 km now resides within the $T'(z, t) = 6°\mathrm{C}$ contour (Figs. 4a,b). This might result from lower NFUS inertial stability (as a result of the weaker tangential winds) causing less resistance to radial flows over this layer. Through a large portion of the middle and upper troposphere ($z = 5$–13 km), the moderate-strength NFUS updrafts in the CCFAD (Fig. 8c) and $\overline{w_{\mathrm{up}}(z)}$ profile (Fig. 8d) are roughly 50% of their counterparts in CTL; these differences are consistent with the weaker azimuthally averaged NFUS updraft core and larger areal coverage of CTL updrafts within the 15-km-wide annulus used to calculate probabilities (Figs. 4c,d). The wider CTL updraft core at peak intensity should primarily result from the merging of a secondary eyewall after 27:00 (Fig. 12 in Part I). The concomitant increase in eyewall upward mass flux might explain why CTL continues to rapidly intensify in the few hours following this merger, even reaching its peak hourly intensification rate during this period (Fig. 1).

b. *Eye*

Although Fig. 8 shows enhanced eyewall downdrafts for CTL relative to NFUS, particularly at peak intensity, we cannot determine whether this difference includes subsidence directed toward the eye, given that our eyewall CCFAD analysis contains little information about the downdrafts' radial location relative to the inner edge. Horizontal plots of upper-level w during RI reveal locally strong downdrafts ($w < -3\,\mathrm{m\,s^{-1}}$) flanking both the inner and outer edges of the CTL and NFUS eyewalls (not shown). These plots also show wavelike patterns of upward and downward motions in the eye, similar to those shown for the simulated Hurricane Andrew, which have been attributed to inertia–gravity wave oscillations with a period of roughly 3 h (Liu et al. 1999; Zhang et al. 2002). Figure 9 shows CCFADs and mean w (areal and 5-h temporal average of updrafts and downdrafts combined) profiles for the CTL and NFUS eye composited from the same times used for Fig. 8. Both simulations generate peak updrafts and downdrafts of nearly equal amplitude ($|w| \approx 1$–$3\,\mathrm{m\,s^{-1}}$) through a deep layer (Figs. 9a,c).

If Wilma's eye warming results primarily from adiabatic descent, as will be shown in Fig. 10, eye-mean w profiles, averaged over time intervals longer than inertia–gravity wave oscillation periods, should reveal subsidence. Indeed, Fig. 9b shows 10–12 $\mathrm{cm\,s^{-1}}$ subsidence for CTL at altitudes near and above the developing warm core (viz., $z > 12$ km) averaged for the 5-h period around 20:00. This is comparable to the 6–10 $\mathrm{cm\,s^{-1}}$ peak subsidence modeled above Andrew's developing warm core (Liu et al. 1999) and the 11-$\mathrm{cm\,s^{-1}}$ subsidence observed in rapidly deepening Gloria's eye (Franklin et al. 1988). NFUS, by contrast, shows weaker mean subsidence of 4–7 $\mathrm{cm\,s^{-1}}$ at 24:00, peaking several kilometers lower (Fig. 9b). The secondary subsidence peak around $z = 3$ km may be associated with Wilma's intensifying low-level inversion (see Fig. 9 in Part I). Around the time of peak intensity (Fig. 9d), CTL develops a deeper layer (above $z = 5$ km) of 10–20 $\mathrm{cm\,s^{-1}}$ eye mean subsidence, and the increased areal fraction of $w < 0$ grid points to 60%–70% over this layer suggests more organized downward motion. NFUS, in contrast, shows little enhancement of eye subsidence near the peak intensity stage, except at the highest levels.

Numerous explanations have been offered for the development of eye subsidence during TC intensification, which may not be mutually exclusive: dynamically induced vertical pressure gradient forces, caused by the balanced response to the vertical decay of the tangential wind field (Smith 1980) or by the sharpening horizontal gradient of the tangential winds (Zhang et al. 2000; Zhang and Kieu 2006), mass lost to moist entraining downdrafts on the inner-eyewall edge (Willoughby 1998), or forced secondary circulations in response to eyewall LHR (Shapiro and Willoughby 1982; Vigh and Schubert 2009; Ohno and Satoh 2015). At peak intensity, the stronger CTL eye subsidence might at least partly result from a dynamic response to its stronger swirling wind field. Nevertheless, the weaker NFUS upper-level eye subsidence observed during the early RI period (Fig. 9b), a time also featuring weaker 99th percentile NFUS eyewall updrafts near the tropopause, provides circumstantial evidence in support of the hypothesis put forward in Heymsfield et al. (2001) and Part II: namely, that upper-level eyewall updrafts enhance eye warming through the compensating subsidence of stratospheric air.

c. *Heat budget analysis in the eye*

After seeing the vertical w profiles in the eye, it is desirable to examine if subsidence is the primary contributor to local eye warming near the tropopause. For this purpose, Fig. 10 shows time tendencies of individual terms in the potential temperature equation:

$$\frac{D\theta}{Dt} = \frac{\partial\theta}{\partial t} + \mathrm{HADV} + \mathrm{VADV}, \tag{1}$$

all averaged over a control volume centered at the CTL upper-level warm anomaly, where $\partial\theta/\partial t$ is the local tendency obtained from time differencing the model output, HADV and VADV are the horizontal and vertical advection terms, respectively, and the material derivative $D\theta/Dt$ includes sources and sinks from cloud microphysics, radiation, and diffusion, as well as calculation errors. To minimize errors, all budget terms are calculated from 5-min-resolution data in Cartesian

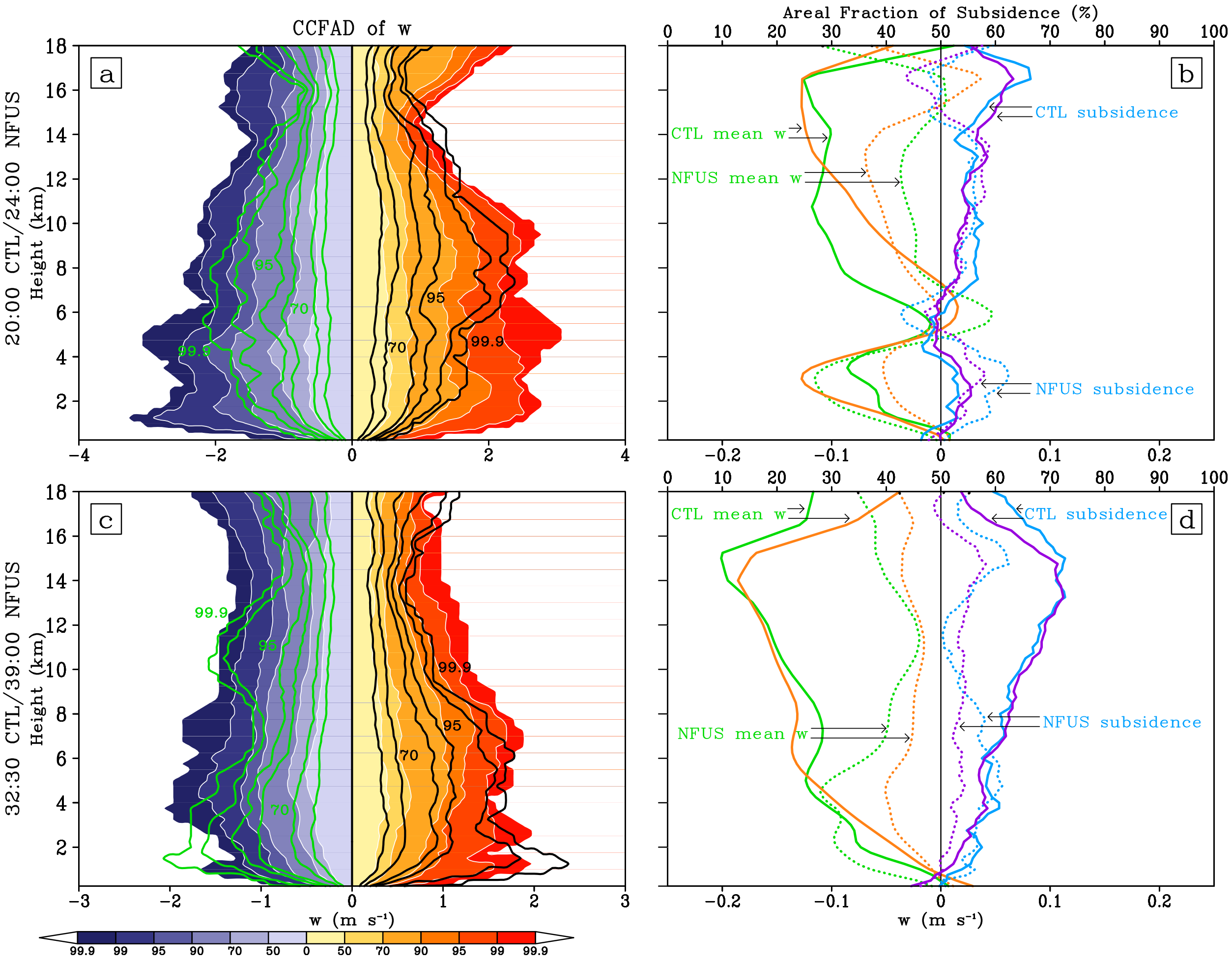

FIG. 9. (a),(c) CCFAD of w as in Fig. 8, but for the eye region (6 km × 6 km box surrounding storm center). (b),(d) Area-averaged mean w (green for 6 km × 6 km box; orange for 10 km × 10 km box) and areal fraction of subsidence ($w < 0\,\mathrm{m\,s^{-1}}$; blue for 6 km × 6 km box; purple for 10 km × 10 km box); CTL (solid) and NFUS (dotted).

coordinates. Radial–height plots of the θ budget terms at selected RI times (not shown) confirm that regions of maximum $\partial\theta/\partial t$ and $\partial T'(z, t)/\partial t$ are spatially collocated.[3] Our analysis shows that adiabatic subsidence warming is indeed the primary contributor to positive local θ tendencies throughout the RI period. The source–sink–error term generally stays negative, and when positive, it remains at least an order of magnitude smaller than $\partial\theta/\partial t$. Repeating this analysis for a wider control volume (e.g., 16 km × 16 km; not shown), the source–sink–error term becomes more substantial, as expected, given the closer proximity to the eyewall interface, but, significantly, subsidence warming remains the only budget term contributing positively to $\partial\theta/\partial t$ (within an order of magnitude) for nearly the full duration of the RI period. These results are consistent with previous heat budget studies of TCs (e.g., Zhang et al. 2002; Stern and Zhang 2013; Ohno and Satoh 2015).

d. Outer rainbands

To investigate how the vertical motion response to reduced LHR in the outer rainbands might differ from that in the eyewall, we plot vertical-motion profiles for the outer rainbands, which contain convective, stratiform, and nonprecipitating regions. Figure 11 shows that the outer rainbands are characterized by weaker updrafts and a smaller area covered by cores relative to the eyewall, confirming the earlier findings of JZL and Black et al. (1996). For both times, CTL exhibits a bimodal updraft profile for CCFAD broadening and for $\overline{w_{\mathrm{up}}}(z)$, with a minimum near $z = 8$ km (Figs. 11a–d). This structure has been documented for tropical convection in

---

[3] Any differences in the warming rate between the θ and $T'(z, t)$ fields would of course result from changes in the pressure fields.

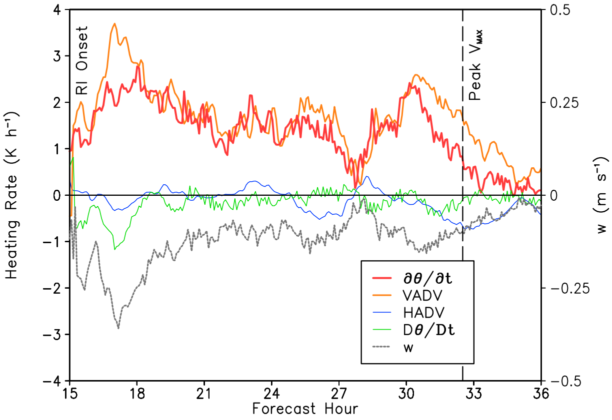

FIG. 10. Time series of various budget terms in the potential temperature tendency equation averaged over a control volume (i.e., 10 km × 10 km; z = 12–16 km) centered at the P_{MIN} centroid. Curves show data that have been smoothed into a 1-h running mean, with equal weighting applied to the 30-min periods prior to and after the indicated time.

modeling studies (Fierro et al. 2009; Wang 2014) and observationally (Yuter and Houze 1995b; Hildebrand et al. 1996; May and Rajopadhyaya 1996), with the upper-level peak attributed to ice LHR processes (Zipser 2003; Romps and Kuang 2010; Fierro et al. 2012).

The CTL rainband vertical motion profiles show little changes from the early RI period to the time of peak V_{MAX}, which should be expected, given that TC intensification is controlled primarily by inner-core convective processes (Ooyama 1982). In the early RI stage (Figs. 11a,b), the NFUS updraft CCFAD and $\overline{w_{\mathrm{up}}(z)}$ profiles are nearly identical to CTL below z = 5 km, roughly the freezing level, but above this altitude, the NFUS updrafts become weaker than CTL, particularly for the strongest 1%. These results suggest that depositional LHR enhances the upper-level updraft peak associated with buoyant convective elements embedded in the outer rainbands. At the time of peak V_{MAX} (Figs. 11c,d), NFUS shows greater CCFAD broadening and a stronger $\overline{w_{\mathrm{up}}(z)}$ relative to CTL, but above z = 12 km these differences become reversed in sign, implying that reduced depositional LHR still has an impact on NFUS updrafts at the upper levels. The larger updraft core fraction in NFUS below z = 12 km suggests that the CCFAD and $\overline{w_{\mathrm{up}}(z)}$ profiles are reflecting a larger areal coverage of vigorous convection in the outer rainbands at this time (Figs. 3c,g).[4] Both CTL and NFUS exhibit a bimodal structure in their downdraft CCFADs, downdraft core fraction, and $\overline{w_{\mathrm{down}}(z)}$ profiles (Fig. 11). Our results support the findings of Yuter and Houze (1995a,b), who reported upper-level downdraft peaks adjacent to upper-level updraft peaks in ordinary tropical convection.

6. Thermodynamic characteristics of convective bursts

In view of the important roles of CBs in the RI of Wilma, we examine the thermodynamic soundings of two selected CBs: one in CTL and the other in NFUS, observed in the developing eyewall 5 h into RI (20:00 in CTL and 24:00 in NFUS). Figures 12a and 12b compare the CB horizontal distribution in relation to upper-level vertical motion and column-integrated total frozen hydrometeors. Note the inward-directed subsidence bands flanking several of the strongest convective cores, peaking at 7 m s^{-1} in CTL and 3 m s^{-1} in NFUS (see arrows), which are similar to observations of Hurricane Bonnie (Heymsfield et al. 2001). Clearly, the CBs in NFUS can still induce subsidence directed into the eye, which is consistent with the fact that NFUS still undergoes RI. For CTL, CB elements and peak column-integrated frozen hydrometeors show a remarkably strong spatial correlation (see arrows). This correlation for NFUS is somewhat weaker, especially for the CB elements in the northern eyewall, which are located several kilometers radially inward from peak column frozen hydrometeors. This displacement results from a greater updraft-core slope angle (with respect to the vertical) over the NFUS northern semicircle (not shown).

Now we zoom in on two CBs, one from each simulation, contained within the 15° azimuthal slices marked by dashed lines in Figs. 12a and 12b. Their height–radial cross sections, given in Figs. 12c and 12d, show an outwardly sloped updraft core peaking in the upper troposphere, an upper-level outflow layer (centered 1 km lower for NFUS), and a deep-layer descent of stratospheric origin flowing down the inner edge of the updraft core. CTL, unlike NFUS, shows a positive θ_e anomaly occurring between the updraft inner edge and core above z = 11 km (Fig. 12c). Similar features have been shown in CTL at RI onset (Fig. 7 in Part II). Since water vapor mixing ratios are extremely small at this altitude, θ_e should be nearly equivalent to θ. The fact that relative humidity associated with the θ_e anomaly region (not shown) is greater than 90% suggests that it may be caused by excessive LHR in the eyewall updrafts that could not be compensated by adiabatic cooling.

Figure 13 compares slantwise environmental soundings in CTL (Figs 13a,b) and NFUS (Figs. 13c,d). For

---

[4] Note for NFUS (Fig. 3g) the extensive band of high radar reflectivity with an embedded CB element cluster in the southern and eastern quadrants, much of which lies outside of 47-km radius, the inner cutoff radius used for rainbands at this time.

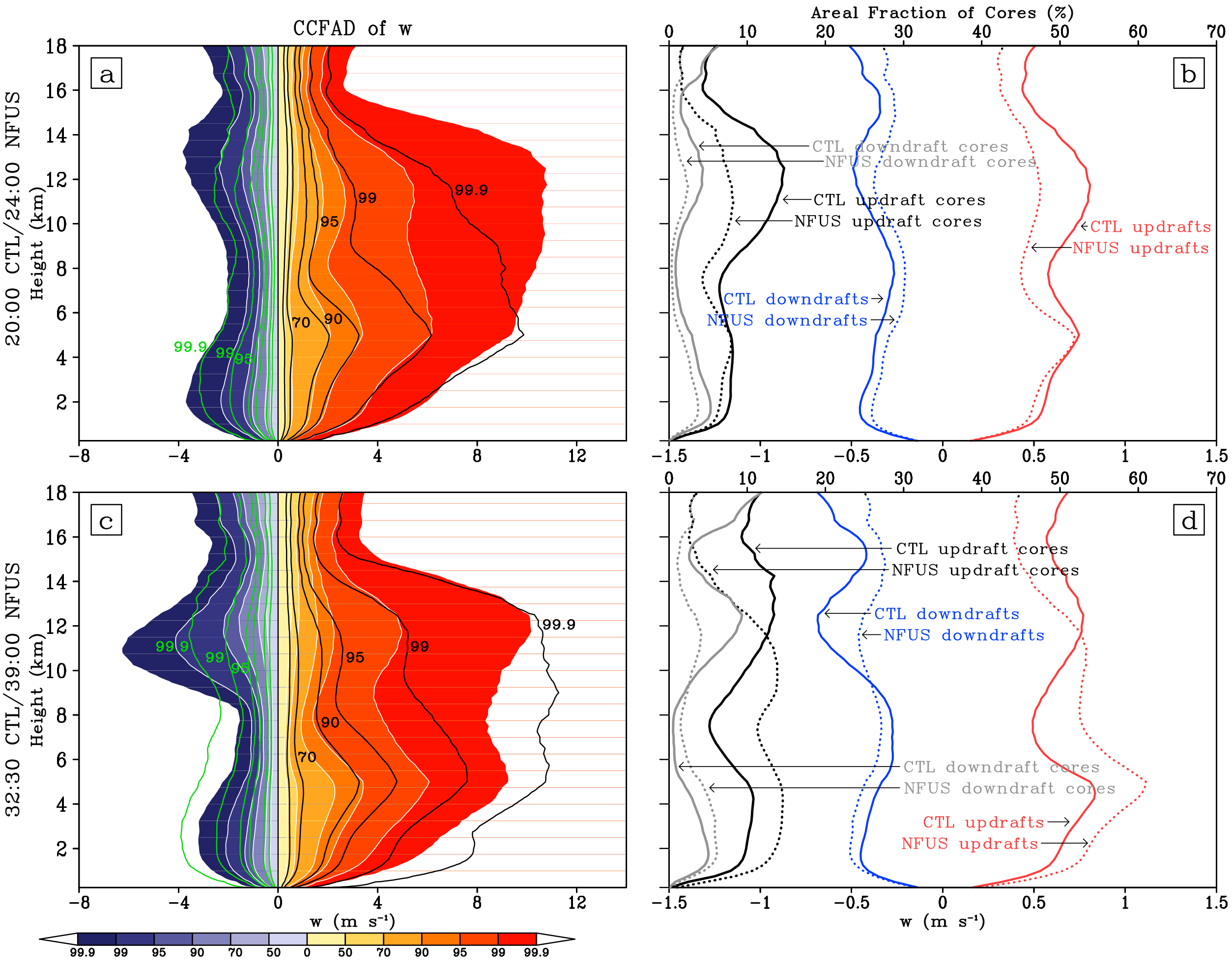

FIG. 11. As in Fig. 8, but for the outer-rainband region.

both simulations, the slantwise sounding, taken through the sloped updraft core to approximate the path of rising parcels in the radial–height plane, closely follows lines of constant θ_e (i.e., 366 K for CTL and 364 K for NFUS) and AAM in a deep layer. The skew T–log$p$ plots show a saturated environment neutral to moist ascent from the MBL through 200 hPa in both CTL (Fig. 13a) and NFUS (Fig. 13c), which is consistent with the wind-induced surface heat exchange (WISHE) hypothesis (Emanuel 1986; Emanuel et al. 1994). Although these soundings are not representative of three-dimensional parcel trajectories, which have been shown to wrap azimuthally around the eyewall (Braun 2002), we demonstrate that a slantwise neutral sounding can also be used to characterize the thermodynamic conditions of a CB.

Nevertheless, substantial evidence for eyewall buoyancy on the convective scale exists, possibly resulting from the temporary steepening of θ_e with respect to AAM surfaces in their vertical tilt (Black et al. 1994), outward parcel displacement into a lower virtual temperature environment by low-level outflow (Braun 2002), or the venting of high-θ_e air out of the eye region (Liu et al. 1999; Persing and Montgomery 2003; Eastin et al. 2005). How might this apparent paradox be resolved? It is possible that LHR has already warmed the updraft cores relative to their surroundings, since this process could occur on time scales too short to be captured by these snapshots of CBs near their peak intensities. Furthermore, the outer edge of the updraft core could still support local buoyancy. Note the rapid decline of environmental θ_e with outward radial extent from the updraft cores (Figs. 12c,d); this being a cloud region, environmental θ_e and θ_{es} should be nearly equivalent. Additionally, an environmental neutral to pseudoadiabatic moist ascent may still support parcel buoyancy when ice LHR processes are accounted for.

To investigate local buoyancy in these CBs, SCAPE is calculated along constant-AAM surfaces running through the center of the updraft cores that closely parallel the slanted sounding lines (Figs. 12c,d). The more-than-threefold increase of eyewall undiluted

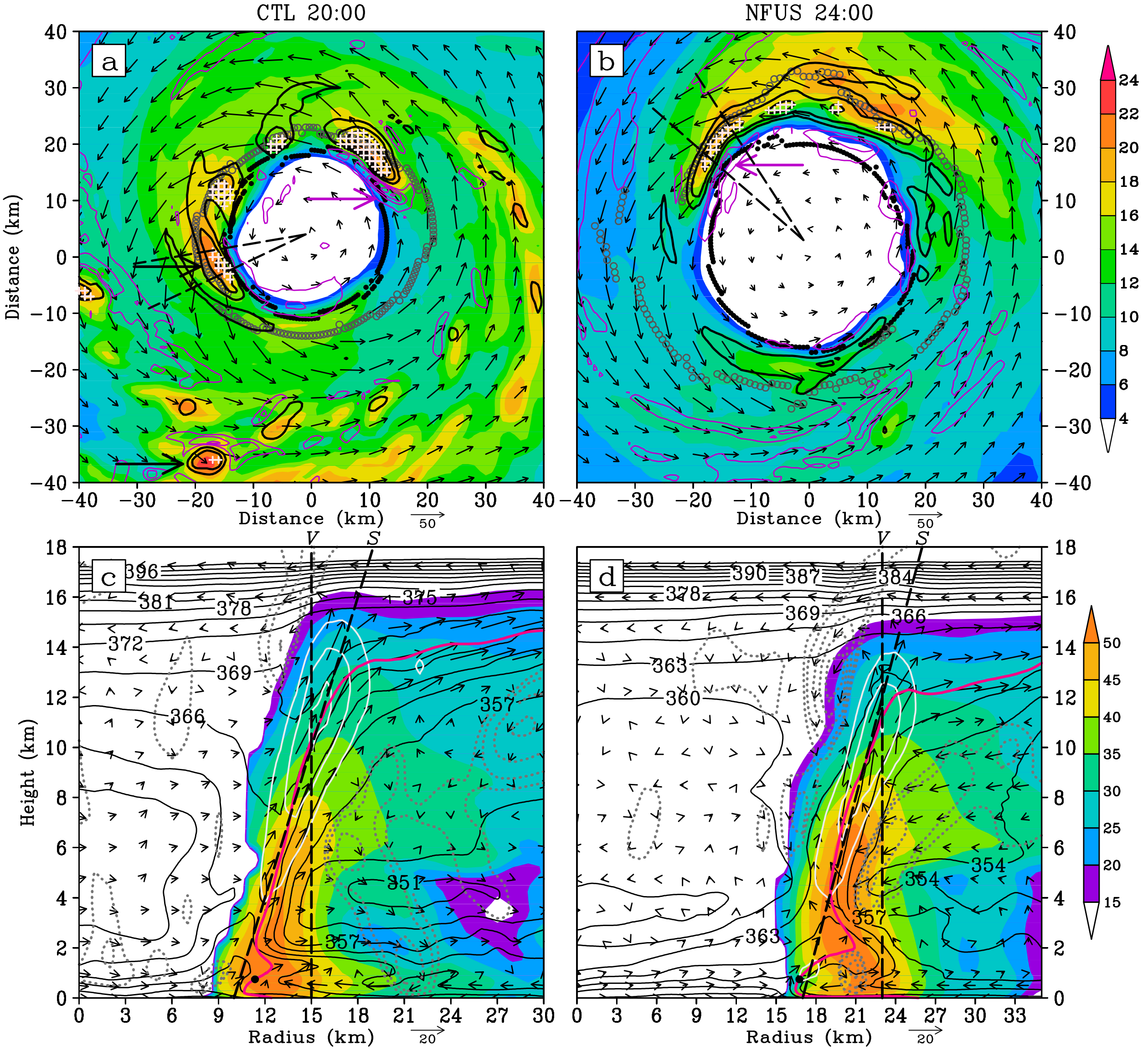

FIG. 12. Total frozen hydrometeors integrated from $z = 6$–16 km (shaded; 10^2 kg kg^{-1}) with horizontal storm-relative-flow vectors (m s^{-1}), vertical motion (upward, black contours, every 5 m s^{-1}; downward, purple contours for −7, −5, −3, and −1 m s^{-1}) and CB elements (light-pink crosses) taken from (a) 20:00 in CTL at $z = 13$ km and (b) 24:00 in NFUS at $z = 11$ km. Local $z = 1$- and 11-km RMWs are marked by black dots and gray circles, respectively. (c),(d) Radial–height cross sections, which show radar reflectivity (shaded; dBZ), θ_e (black contours; K), vertical motion (upward, white contours, every 5 m s^{-1}; downward, dotted gray contours for −4, −3, −2, −1, and −0.5 m s^{-1}), and AAM (magenta contour, 5×10^5 s^{-1}; 1.4 for CTL; 2.0 for NFUS), with in-plane-flow vectors (vertical motions multiplied by 2), all azimuthally averaged over 15° slices bounded by dashed lines in (a) and (b), respectively. Slanted and vertical sounding lines are labeled with "S" and "V," respectively. Black dots in (c) and (d) mark parcel lifting points used for SCAPE calculations.

SCAPE for CTL with ice LHR allowed over that of NFUS with ice LHR neglected (Figs. 13a,c) suggests that parcel warming from the latent heat of fusion (through both depositional and freezing processes) might be an important contributor to local buoyancy in the eyewall. While the neglect of freezing processes in the NFUS SCAPE calculation might render this value a bit conservative, it is still sufficient to generate $w_{\max} > 17$ m s^{-1}.

Figures 13b and 13d compare profiles of vertical motion, cloud species mixing ratios, and θ_e between the two simulations. In general, the cloud species profiles are fairly similar, with cloud ice and snow peaking in the 150–300-hPa layer and graupel, formed by the riming of

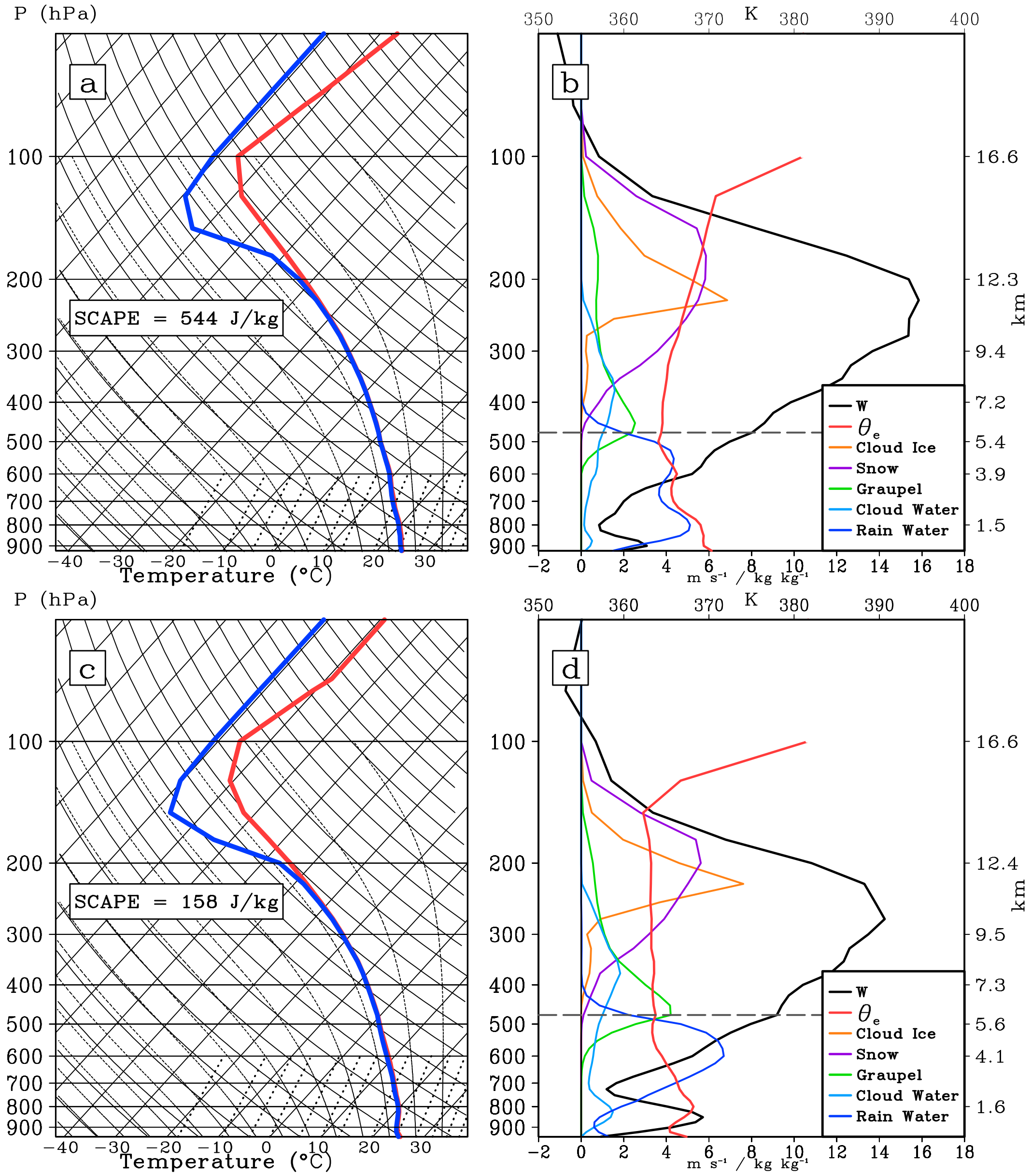

FIG. 13. Skew T–log$p$ diagrams for (a) CTL and (c) NFUS, with environmental variables taken from slanted sounding lines (S), and with SCAPE computed along constant-AAM lines, both from Fig. 12. Profiles along the slanted sounding lines of vertical motion (m s^{-1}), θ_e (K), and cloud species mixing ratios [kg kg^{-1}; ($\times 10^5$) for cloud ice, ($\times 10^3$) for snow, graupel, cloud water, and rain] for (b) CTL and (d) NFUS. The dashed gray line marks the approximate freezing-level height. The top of each panel marks the 50-hPa level.

ice and snow and the freezing of raindrops, peaking just above the freezing level, where supercooled water is more abundant. The vertical motion profiles show a similar shape with peak magnitudes of 16 m s^{-1} for CTL and 14 m s^{-1} for NFUS but note that the CTL updraft peaks 1.5 km higher, closer to the maximum snow and ice mixing ratios. Possible entrainment effects and negative perturbation pressure gradient forces, both neglected in our analysis, might account for the peak CTL and NFUS updraft magnitudes falling short of the $w_{\max}$ predicted by SCAPE. Despite the saturated soundings over the 800–500-hPa layer, the decline in θ_e over this layer for both simulations may result from weak entrainment, given the proximity to the low-θ_e regions just outside of the updrafts (cf. Figs. 12c,d and Fig. 13). Also noteworthy is the nearly constant NFUS θ_e profile over the 550–150-hPa layer, which contrasts with the CTL profile showing a gradual θ_e increase

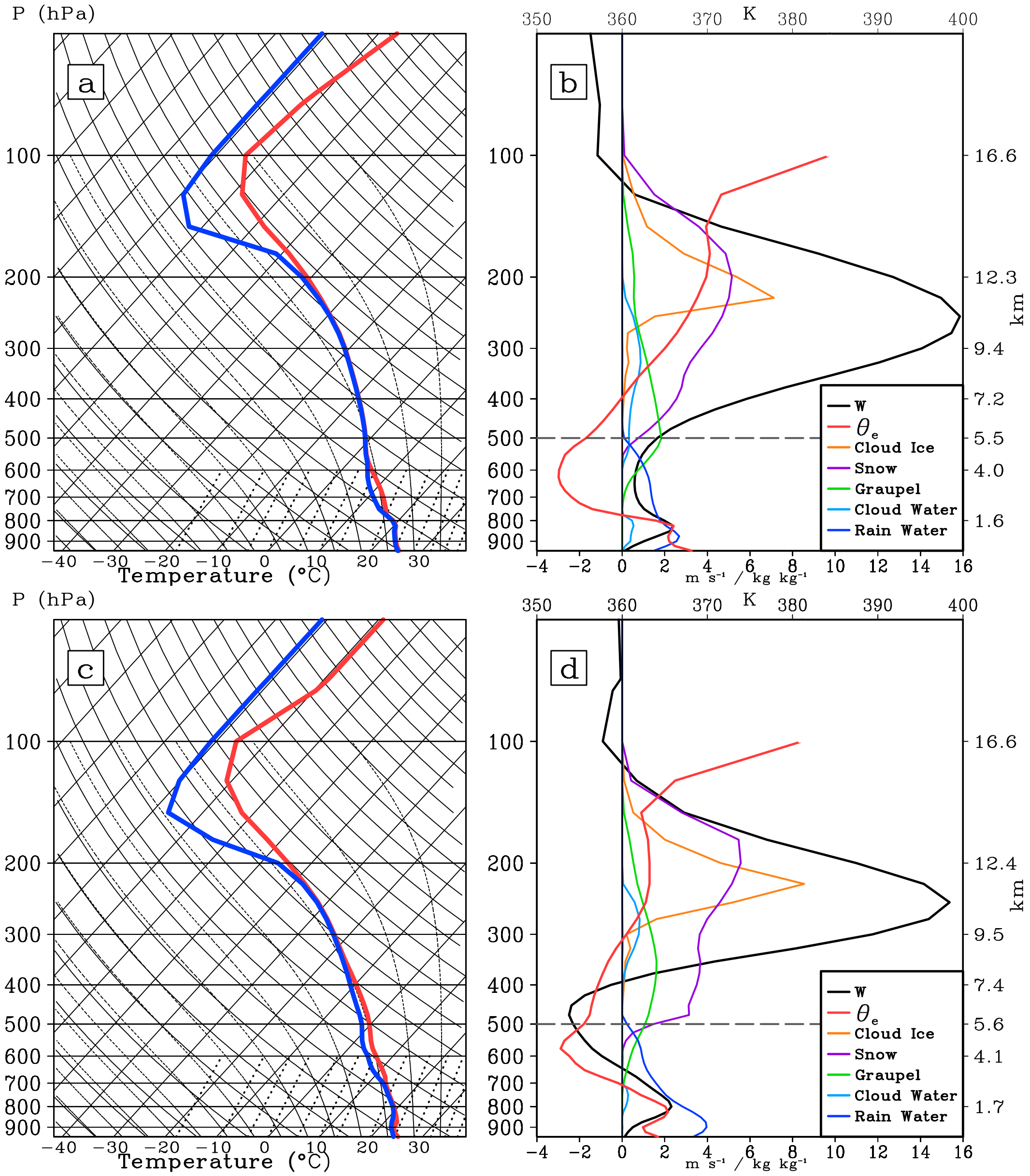

FIG. 14. As in Fig. 13, but for vertical sounding lines (V) from Fig. 12.

above the midlevel minimum. Since θ_e is conserved with respect to the latent heat of vaporization, the absence of a θ_e increase at higher levels in NFUS is consistent with the removal of the fusion component of L_d.

To illustrate how slantwise, as opposed to vertical, soundings through the eyewall provide a more realistic representation of the thermodynamic environment, Fig. 14 shows soundings taken along vertical lines marked "V" in Figs. 12c and 12d, which extend downward from the upper portions of the updraft cores. The nearly dry adiabatic but saturated layer in the 750–800-hPa layer in Fig. 14a would imply an absolutely unstable condition for upright motion, but here it just reflects an upward transition from the MBL to a θ_e-minimum region near $z = 4$ km characterized by subsaturated conditions (cf. Figs. 12c and 14a,b). Above the θ_e minimum, the sounding penetrates into the higher-θ_e updraft core, with a stable lapse rate between 400 and 250 hPa. The NFUS vertical soundings (Figs. 14c,d) show similar trends, with an increase in θ_e now evident with upward extent from the unsaturated midlevel-downdraft region into the saturated updraft core. Note that, unlike for CTL, θ_e no longer increases above

$z = 11$ km, where cloud ice and snow peak and where depositional growth should be maximized.

7. Summary and concluding remarks

In this study, the impacts of the latent heat of fusion on the RI of Hurricane Wilma (2005) are examined by comparing a 72-h control simulation of the storm to a sensitivity simulation in which the latent heat of deposition is reduced by removing the fusion component. Although the NFUS storm still undergoes RI, the RI onset is delayed by 4 h, the duration is 5 h shorter, and the average deepening rate is reduced (3.0 vs 3.7 hPa h^{-1} in CTL). For both storms, the RI period is characterized by lowering upper-level isentropic surfaces and the development of anomalous warming near $z = 14$ km in the eye. At the time of peak intensity, the NFUS storm is 30 hPa weaker in P_{MIN}, with upper-level warming reduced by 8°C.

During the pre-RI and RI periods, NFUS generates fewer CB elements inside the $z = 11$-km RMW. These results are supported by CCFAD diagrams composited from a 5-h period during the early portion of RI that feature stronger eyewall updrafts in CTL, most notably in the upper troposphere for the highest percentiles of the velocity range. During this period, CTL also shows enhanced mean subsidence above $z = 12$ km in the eye. By peak intensity, CTL has developed a stronger secondary circulation compared to NFUS. For both simulations, the outer rainbands are characterized by weaker vertical motion relative to the eyewall, although depositional heating appears to enhance upper-level updrafts and the associated compensating subsidence for the rainband convective elements as well.

Soundings taken through the updraft cores of selected RI-phase CBs for both CTL and NFUS reveal neutral to slantwise moist ascent. But updrafts peak 1.5 km higher for CTL, closer to the highest cloud ice and snow mixing ratios, despite the fact that the thermodynamic environment and updraft intensity are nearly identical below the freezing level for the NFUS CB. SCAPE calculations reveal ice LHR processes to be an important factor in generating sufficient conditional instability to support CB updrafts in the eyewall. This finding is not incompatible with the slantwise neutral soundings because of (i) the possibility that the Eulerian analysis is sampling a local environment already warmed by LHR and (ii) the possibility that a slantwise neutral sounding can still support positive buoyancy when parcel temperature calculations account for ice processes.

In conclusion, the above results support our hypothesis that depositional LHR in the eyewall facilitates TC intensification through the enhancement of CB activity. The extreme altitude reached by CB updrafts allows for the downward displacement of lower-stratospheric air in compensating subsidence currents. RI commences once an upper-level cyclonic circulation can develop, which acts to protect warming over the eye from ventilation by environmental flows. The CB-induced subsidence warming then begins to concentrate to form an upper-level warm core, which hydrostatically induces surface pressure falls in the eye region.

We should mention alternate hypotheses, put forward by some other studies, on the role of CBs, or even the importance of deep convection altogether, in the onset and maintenance of TC rapid intensification. For his Hurricane Dennis simulation, Rogers (2010) found that an inner-core CB outbreak 6–12 h prior to RI onset enhanced the low-level updraft mass flux, strengthening the secondary circulation. The accompanying increase in inertial stability, resulting from the cooperative intensification of the tangential wind field, placed the vortex in a region of increased diabatic heating conversion efficiency, which allowed RI to proceed. Interestingly, although Rogers (2010) emphasized the enhanced background secondary circulation as the direct impact of CBs on vortex-scale intensification, he did find a spike in downward mass flux in the upper-level eye accompanying the CB outbreak, which was followed by eye warming. McFarquhar et al. (2012), on the other hand, identified strengthening of the 99.9th percentile updrafts at $z = 14$ km as the precursor to Dennis's RI. Although their study found that weak updrafts accomplished the bulk of the total inner-core LHR, these results do not necessarily discount the importance of CBs (and their compensating subsidence) in maintaining RI, since local LHR-induced warming in Wilma's eyewall appears to be quickly compensated for by adiabatic cooling (Part II). Other studies have emphasized the role of shallow convection, diagnosed by ringlike structures in 37-GHz microwave imagery (Kieper and Jiang 2012) or by Tropical Rainfall Measuring Mission Precipitation Radar (TRMM PR; Zagrodnik and Jiang 2014), in initiating RI episodes. Although this work appears to contradict our findings, we wish to point out that the composited satellite observations used in Zagrodnik and Jiang (2014) included cases where an RI period had commenced up to 12 h before the overpass. It is possible that, for some TCs, increasingly organized shallow convection simply represents an intensifying secondary circulation triggered by transient deep convective episodes that might not be captured by periodic satellite overpasses.

Finally, Wilma's record-breaking intensity and near-ideal environmental conditions for intensification lead us to the obvious question of how generally our results might apply to other TCs. Clearly, future studies of ice process LHR impacts on weaker storms undergoing RI in less favorable environments would be helpful, as would the testing of other microphysics schemes and the accumulation of more observations validating the microphysics scheme parameterizations. Nevertheless, this study highlights the important contribution of the latent heat of fusion to the RI of a strong TC, given favorable environmental conditions.

Acknowledgments. This work was supported by ONR Grant N000141410143 and NASA Grant NNX12AJ78G.

APPENDIX

Calculation of SCAPE

SCAPE is calculated from azimuthally averaged variables following Craig and Gray (1996) using the integral

$$\mathrm{SCAPE} = g\int_{\mathrm{LCL}}^{\mathrm{LNB}} \left(\frac{T_{vp} - T_{ve}}{T_{ve}}\right)_{\mathrm{AAM}} dz\,, \tag{A1}$$

where T_{vp} and T_{ve} denote parcel and environmental virtual temperatures, respectively, and g is the gravitational constant. Although the limits of integration run from the lifting condensation level (LCL) to the LNB, negative areas between these limits (also referred to as convective inhibition) are not included in the summation. SCAPE is equivalent to CAPE, except for the fact that the vertical coordinate z follows surfaces of constant absolute angular momentum, given by

$$\mathrm{AAM} = r\left(V + \frac{fr}{2}\right), \tag{A2}$$

where r is the radius, V is the tangential wind, and f is the Coriolis parameter. The SCAPE integration is terminated for AAM surfaces extending more than 30 km beyond the lifted parcel radius prior to the LNB being reached. Enforcing this limit ensures that, for parcels lifted in the eyewall (the region of focus for our study), the SCAPE integration does not extend radially beyond a path physically consistent with the modeled slantwise convection, given the tendency for AAM surfaces to become nearly horizontal in the upper troposphere. A parcel lifting height of $z = 0.75$ km, chosen for its close proximity to the top of the MBL, is used for both CTL and NFUS. Parcel AAM is kept constant above this height by interpolating through the radial–height grid.

Lifted-parcel temperatures for both CTL and NFUS are calculated using reversible thermodynamics (all condensates retained in rising parcels). While the effects of entrainment are not considered here, they should be less significant for the inner-core region, given the high ambient midtropospheric relative humidity (Molinari et al. 2012); furthermore, any overestimate of SCAPE based on neglecting entrainment should be partially compensated by (or perhaps overcompensated by) our neglecting hydrometeor fallouts from rising parcels. Since following a reversible adiabat requires the tracking of hydrometeor mixing ratios, we utilize a simplified three-species (vapor, liquid, and ice) microphysics parameterization outlined in Bryan and Fritsch (2004). Thus, while the initial parcel properties are obtained from the WRF Model output, the computation of parcel temperatures along AAM surfaces uses a simplified alternative to the Thompson microphysics. Details of this three-species scheme can be found in Bryan and Fritsch (2004). In summary, it assumes vapor saturation with respect to water between the LCL and the freezing level, saturation with respect to ice for temperatures below −40°C, and for the layer in between, the calculation of supercooled liquid and ice mixing ratios uses a linear weighting technique.

Lifted-parcel temperatures are computed using

$$\frac{D\ln\theta}{Dt} = \left(\frac{R_m}{c_{pml}} - \frac{R}{c_p}\right)\frac{D\ln p}{Dt} + \frac{L_v}{c_{pml}T}\frac{Dr_l}{Dt} + \frac{L_d}{c_{pml}T}\frac{Dr_i}{Dt}, \tag{A3}$$

following Eqs. (4) and (8) in Bryan and Fritsch (2004), with mixing ratio r designated by the subscript l or i for liquid or ice, respectively; L_v as the latent heat of vaporization; L_d as the latent heat of deposition; R_m and R as the gas constants for moist and dry air, respectively; c_{pml} as the total specific heat at constant pressure (weighted by vapor, liquid, and ice mixing ratios); and c_p as the specific heat of dry air at constant pressure. For CTL, ice production above the freezing level allows for parcel warming by the latent heat of fusion ($L_f = L_d - L_v$) both for freezing ($Dr_i = -Dr_l$) and for deposition ($Dr_i > 0$, $Dr_l = 0$).[5] However, for NFUS, ice production is not permitted, forcing the accumulation of supercooled condensate above the freezing level, thus not allowing L_f to warm the parcel by either freezing or deposition processes.

---

[5] Using reversible thermodynamics with ice processes included is considered the most accurate method for calculating undiluted CAPE in the tropical environment within the constraints of parcel theory (Williams and Renno 1993), although calculations with partial hydrometeor fallout have been performed on occasion (Romps and Kuang 2010).

REFERENCES

Black, M. L., R. W. Burpee, and F. D. Marks Jr., 1996: Vertical motion characteristics of tropical cyclones determined with airborne Doppler radial velocities. *J. Atmos. Sci.*, **53**, 1887–1909, doi:10.1175/1520-0469(1996)053<1887:VMCOTC>2.0.CO;2.

Black, R. A., H. B. Bluestein, and M. L. Black, 1994: Unusually strong vertical motions in a Caribbean hurricane. *Mon. Wea. Rev.*, **122**, 2722–2739, doi:10.1175/1520-0493(1994)122<2722:USVMIA>2.0.CO;2.

Braun, S. A., 2002: A cloud-resolving simulation of Hurricane Bob (1991): Storm structure and eyewall buoyancy. *Mon. Wea. Rev.*, **130**, 1573–1592, doi:10.1175/1520-0493(2002)130<1573:ACRSOH>2.0.CO;2.

Bryan, G. H., and J. M. Fritsch, 2004: A reevaluation of ice–liquid water potential temperature. *J. Atmos. Sci.*, **132**, 2421–2431, doi:10.1175/1520-0493(2004)132<2421:AROIWP>2.0.CO;2.

Chen, H., and D.-L. Zhang, 2013: On the rapid intensification of Hurricane Wilma (2005). Part II: Convective bursts and the upper-level warm core. *J. Atmos. Sci.*, **70**, 146–162, doi:10.1175/JAS-D-12-062.1.

——, ——, J. Carton, and R. Atlas, 2011: On the rapid intensification of Hurricane Wilma (2005). Part I: Model prediction and structural changes. *Wea. Forecasting*, **26**, 885–901, doi:10.1175/WAF-D-11-00001.1.

Craig, G. C., and S. L. Gray, 1996: CISK or WISHE as the mechanism for tropical cyclone intensification. *J. Atmos. Sci.*, **53**, 3528–3540, doi:10.1175/1520-0469(1996)053<3528:COWATM>2.0.CO;2.

Eastin, M. D., W. M. Gray, and P. G. Black, 2005: Buoyancy of convective vertical motions in the inner core of intense hurricanes. Part II: Case studies. *Mon. Wea. Rev.*, **133**, 209–227, doi:10.1175/MWR-2849.1.

Emanuel, K. A., 1986: An air–sea interaction theory for tropical cyclones. Part I: Steady-state maintenance. *J. Atmos. Sci.*, **43**, 585–604, doi:10.1175/1520-0469(1986)043<0585:AASITF>2.0.CO;2.

——, J. D. Neelin, and C. S. Bretherton, 1994: On large-scale circulations in convecting atmospheres. *Quart. J. Roy. Meteor. Soc.*, **120**, 1111–1143, doi:10.1002/qj.49712051902.

Fierro, A. O., and J. M. Reisner, 2011: High-resolution simulation of the electrification and lightning of Hurricane Rita during the period of rapid intensification. *J. Atmos. Sci.*, **68**, 477–494, doi:10.1175/2010JAS3659.1.

——, J. Simpson, M. A. LeMone, J. M. Straka, and B. F. Smull, 2009: On how hot towers fuel the Hadley cell: An observational and modeling study of line-organized convection in the equatorial trough from TOGA COARE. *J. Atmos. Sci.*, **66**, 2730–2746, doi:10.1175/2009JAS3017.1.

——, E. J. Zipser, M. A. LeMone, J. M. Straka, and J. Simpson, 2012: Tropical oceanic hot towers: Need they be undilute to transport energy from the boundary layer to the upper troposphere effectively? An answer based on trajectory analysis of a simulation of a TOGA COARE convective system. *J. Atmos. Sci.*, **69**, 195–213, doi:10.1175/JAS-D-11-0147.1.

Franklin, J. L., S. J. Lord, and F. D. Marks Jr., 1988: Dropwindsonde and radar observations of the eye of Hurricane Gloria (1985). *Mon. Wea. Rev.*, **116**, 1237–1244, doi:10.1175/1520-0493(1988)116<1237:DAROOT>2.0.CO;2.

——, R. J. Pasch, L. A. Avila, J. L. Beven II, M. B. Lawrence, S. R. Stewart, and E. S. Blake, 2006: Atlantic Hurricane season of 2004. *Mon. Wea. Rev.*, **134**, 981–1025, doi:10.1175/MWR3096.1.

Frisius, T., and D. Schönemann, 2012: An extended model for the potential intensity of tropical cyclones. *J. Atmos. Sci.*, **69**, 641–661, doi:10.1175/JAS-D-11-064.1.

Guimond, S. R., G. M. Heymsfield, and F. J. Turk, 2010: Multiscale observations of Hurricane Dennis (2005): The effects of hot towers on rapid intensification. *J. Atmos. Sci.*, **67**, 633–654, doi:10.1175/2009JAS3119.1.

Hack, J. J., and W. H. Schubert, 1986: Nonlinear response of atmospheric vortices to heating by organized cumulus convection. *J. Atmos. Sci.*, **43**, 1559–1573, doi:10.1175/1520-0469(1986)043<1559:NROAVT>2.0.CO;2.

Heymsfield, G. M., J. B. Halverson, J. Simpson, L. Tian, and T. P. Bui, 2001: ER-2 Doppler radar investigations of the eyewall of Hurricane Bonnie during the Convection and Moisture Experiment-3. *J. Appl. Meteor.*, **40**, 1310–1330, doi:10.1175/1520-0450(2001)040<1310:EDRIOT>2.0.CO;2.

Hildebrand, P. H., and Coauthors, 1996: The ELDORA/ASTRAIA airborne Doppler weather radar: High-resolution observations from TOGA COARE. *Bull. Amer. Meteor. Soc.*, **77**, 213–232, doi:10.1175/1520-0477(1996)077<0213:TEADWR>2.0.CO;2.

Holliday, C. R., and A. H. Thompson, 1979: Climatological characteristics of rapidly intensifying typhoons. *Mon. Wea. Rev.*, **107**, 1022–1034, doi:10.1175/1520-0493(1979)107<1022:CCORIT>2.0.CO;2.

Jorgensen, D. P., E. J. Zipser, and M. A. LeMone, 1985: Vertical motions in intense hurricanes. *J. Atmos. Sci.*, **42**, 839–856, doi:10.1175/1520-0469(1985)042<0839:VMIIH>2.0.CO;2.

Kaplan, J., and M. DeMaria, 2003: Large-scale characteristics of rapidly intensifying tropical cyclones in the North Atlantic basin. *Wea. Forecasting*, **18**, 1093–1108, doi:10.1175/1520-0434(2003)018<1093:LCORIT>2.0.CO;2.

Kieper, M., and H. Jiang, 2012: Predicting tropical cyclone rapid intensification using the 37 GHz ring pattern identified from passive microwave instruments. *Geophys. Res. Lett.*, **39**, L13804, doi:10.1029/2012GL052115.

Kieu, C. Q., H. Chen, and D.-L. Zhang, 2010: An examination of the pressure–wind relationship for intense tropical cyclones. *Wea. Forecasting*, **25**, 895–907, doi:10.1175/2010WAF2222344.1.

Lawrence, M. B., B. M. Mayfield, L. A. Avila, R. J. Pasch, and E. N. Rappaport, 1998: Atlantic hurricane season of 1995. *Mon. Wea. Rev.*, **126**, 1124–1151, doi:10.1175/1520-0493(1998)126<1124:AHSO>2.0.CO;2.

——, L. A. Avila, J. L. Beven, J. L. Franklin, J. L. Guiney, and R. J. Pasch, 2001: Atlantic hurricane season of 1999. *Mon. Wea. Rev.*, **129**, 3057–3084, doi:10.1175/1520-0493(2001)129<3057:AHSO>2.0.CO;2.

Liu, Y., D.-L. Zhang, and M. K. Yau, 1999: A multiscale numerical study of Hurricane Andrew (1992). Part II: Kinematics and inner-core structures. *Mon. Wea. Rev.*, **127**, 2597–2616, doi:10.1175/1520-0493(1999)127<2597:AMNSOH>2.0.CO;2.

Marks, F. D., Jr., and R. A. Houze Jr., 1987: Inner core structure of Hurricane Alicia from airborne Doppler radar observations. *J. Atmos. Sci.*, **44**, 1296–1317, doi:10.1175/1520-0469(1987)044<1296:ICSOHA>2.0.CO;2.

May, P. T., and D. K. Rajopadhyaya, 1996: Wind profiler observations of vertical motion and precipitation microphysics of a tropical squall line. *Mon. Wea. Rev.*, **124**, 621–633, doi:10.1175/1520-0493(1996)124<0621:WPOOVM>2.0.CO;2.

McFarquhar, G. M., B. F. Jewett, M. S. Gilmore, S. W. Nesbitt, and T.-L. Hsieh, 2012: Vertical velocity and microphysical distributions related to rapid intensification in a simulation of Hurricane Dennis (2005). *J. Atmos. Sci.*, **69**, 3515–3534, doi:10.1175/JAS-D-12-016.1.

Molinari, J., and D. Vollaro, 2010: Rapid intensification of a sheared tropical storm. *Mon. Wea. Rev.*, **138**, 3869–3885, doi:10.1175/2010MWR3378.1.

——, P. Moore, and V. Idone, 1999: Convective structure of hurricanes as revealed by lightning locations. *Mon. Wea. Rev.*, **127**, 520–534, doi:10.1175/1520-0493(1999)127<0520:CSOHAR>2.0.CO;2.

——, D. M. Romps, D. Vollaro, and L. Nguyen, 2012: CAPE in tropical cyclones. *J. Atmos. Sci.*, **69**, 2452–2463, doi:10.1175/JAS-D-11-0254.1.

Ohno, T., and M. Satoh, 2015: On the warm core of a tropical cyclone formed near the tropopause. *J. Atmos. Sci.*, **72**, 551–571, doi:10.1175/JAS-D-14-0078.1.

Ooyama, K. V., 1982: Conceptual evolution of the theory and modeling of the tropical cyclone. *J. Meteor. Soc. Japan*, **60**, 369–380.

Persing, J., and M. T. Montgomery, 2003: Hurricane superintensity. *J. Atmos. Sci.*, **60**, 2349–2371, doi:10.1175/1520-0469(2003)060<2349:HS>2.0.CO;2.

Price, C., M. Asfur, and Y. Yair, 2009: Maximum hurricane intensity preceded by increase in lightning frequency. *Nat. Geosci.*, **2**, 329–332, doi:10.1038/ngeo477.

Rodgers, E. B., W. S. Olson, V. M. Karyampudi, and H. F. Pierce, 1998: Satellite-derived latent heating distribution and environmental influences in Hurricane Opal (1995). *Mon. Wea. Rev.*, **126**, 1229–1247, doi:10.1175/1520-0493(1998)126<1229:SDLHDA>2.0.CO;2.

——, ——, J. Halverson, J. Simpson, and H. Pierce, 2000: Environmental forcing of Supertyphoon Paka's (1997) latent heat structure. *J. Appl. Meteor.*, **39**, 1983–2006, doi:10.1175/1520-0450(2001)040<1983:EFOSPS>2.0.CO;2.

Rogers, R. F., 2010: Convective-scale structure and evolution during a high-resolution simulation of tropical cyclone rapid intensification. *J. Atmos. Sci.*, **67**, 44–70, doi:10.1175/2009JAS3122.1.

——, P. Reasor, and S. Lorsolo, 2013: Airborne Doppler observations of the inner-core structural differences between intensifying and steady-state tropical cyclones. *Mon. Wea. Rev.*, **141**, 2970–2991, doi:10.1175/MWR-D-12-00357.1.

——, ——, and J. A. Zhang, 2015: Multiscale structure and evolution of Hurricane Earl (2010) during rapid intensification. *Mon. Wea. Rev.*, **143**, 536–562, doi:10.1175/MWR-D-14-00175.1.

Rogers, R. R., and M. K. Yau, 1989: *A Short Course in Cloud Physics*. 3rd ed. Elsevier, 290 pp.

Romps, D. M., and Z. Kuang, 2010: Do undiluted convective plumes exist in the upper tropical troposphere? *J. Atmos. Sci.*, **67**, 468–484, doi:10.1175/2009JAS3184.1.

Shapiro, L. J., and H. E. Willoughby, 1982: The response of balanced hurricanes to local sources of heat and momentum. *J. Atmos. Sci.*, **39**, 378–394, doi:10.1175/1520-0469(1982)039<0378:TROBHT>2.0.CO;2.

Smith, R. K., 1980: Tropical cyclone eye dynamics. *J. Atmos. Sci.*, **37**, 1227–1232, doi:10.1175/1520-0469(1980)037<1227:TCED>2.0.CO;2.

Stern, D. P., and F. Zhang, 2013: How does the eye warm? Part I: A potential temperature budget analysis of an idealized tropical cyclone. *J. Atmos. Sci.*, **70**, 73–90, doi:10.1175/JAS-D-11-0329.1.

Stevenson, S. N., K. L. Corbosiero, and J. Molinari, 2014: The convective evolution and rapid intensification of Hurricane Earl (2010). *Mon. Wea. Rev.*, **142**, 4364–4380, doi:10.1175/MWR-D-14-00078.1.

Thompson, G., R. M. Rasmussen, and K. Manning, 2004: Explicit forecasts of winter precipitation using an improved bulk microphysics scheme. Part I: Description and sensitivity analysis. *Mon. Wea. Rev.*, **132**, 519–542, doi:10.1175/1520-0493(2004)132<0519:EFOWPU>2.0.CO;2.

——, P. R. Field, R. M. Rasmussen, and W. D. Hall, 2008: Explicit forecasts of winter precipitation using an improved bulk microphysics scheme. Part II: Implementation of a new snow parameterization. *Mon. Wea. Rev.*, **136**, 5095–5115, doi:10.1175/2008MWR2387.1.

Vigh, J. L., and W. H. Schubert, 2009: Rapid development of the tropical cyclone warm core. *J. Atmos. Sci.*, **66**, 3335–3350, doi:10.1175/2009JAS3092.1.

Wang, H., and Y. Wang, 2014: A numerical study of Typhoon Megi (2010). Part I: Rapid intensification. *Mon. Wea. Rev.*, **142**, 29–48, doi:10.1175/MWR-D-13-00070.1.

Wang, Z., 2014: Characteristics of convective processes and vertical velocity from the tropical wave to tropical cyclone stage in a high-resolution numerical model simulation of Tropical Cyclone Fay (2008). *J. Atmos. Sci.*, **71**, 896–915, doi:10.1175/JAS-D-13-0256.1.

Williams, E., and N. Renno, 1993: An analysis of the conditional instability of the tropical atmosphere. *Mon. Wea. Rev.*, **121**, 21–36, doi:10.1175/1520-0493(1993)121<0021:AAOTCI>2.0.CO;2.

Willoughby, H. E., 1998: Tropical cyclone eye thermodynamics. *Mon. Wea. Rev.*, **126**, 3053–3067, doi:10.1175/1520-0493(1998)126<3053:TCET>2.0.CO;2.

Yuter, S. E., and R. A. Houze Jr., 1995a: Three-dimensional kinematic and microphysical evolution of Florida cumulonimbus. Part I: Spatial distribution of updrafts, downdrafts, and precipitation. *Mon. Wea. Rev.*, **123**, 1921–1940, doi:10.1175/1520-0493(1995)123<1921:TDKAME>2.0.CO;2.

——, and ——, 1995b: Three-dimensional kinematic and microphysical evolution of Florida cumulonimbus. Part II: Frequency distributions of vertical velocity, reflectivity, and differential reflectivity. *Mon. Wea. Rev.*, **123**, 1941–1963, doi:10.1175/1520-0493(1995)123<1941:TDKAME>2.0.CO;2.

Zagrodnik, J. P., and H. Jiang, 2014: Rainfall, convection, and latent heating distributions in rapidly intensifying tropical cyclones. *J. Atmos. Sci.*, **71**, 2789–2809, doi:10.1175/JAS-D-13-0314.1.

Zhang, D.-L., and C. Q. Kieu, 2006: Potential vorticity diagnosis of a simulated hurricane. Part II: Quasi-balanced contributions to forced secondary circulations. *J. Atmos. Sci.*, **63**, 2898–2914, doi:10.1175/JAS3790.1.

——, and H. Chen, 2012: Importance of the upper-level warm core in the rapid intensification of a tropical cyclone. *Geophys. Res. Lett.*, **39**, L02806.

——, Y. Liu, and M. K. Yau, 2000: A multiscale numerical study of Hurricane Andrew (1992). Part III: Dynamically induced vertical motion. *Mon. Wea. Rev.*, **128**, 3772–3788, doi:10.1175/1520-0493(2001)129<3772:AMNSOH>2.0.CO;2.

——, ——, and ——, 2002: A multiscale numerical study of Hurricane Andrew (1992): Part V: Inner-core thermodynamics. *Mon. Wea. Rev.*, **130**, 2745–2763, doi:10.1175/1520-0493(2002)130<2745:AMNSOH>2.0.CO;2.

Zhu, T., and D.-L. Zhang, 2006: Numerical simulation of Hurricane Bonnie (1998). Part II: Sensitivity to cloud microphysical processes. *J. Atmos. Sci.*, **63**, 109–126, doi:10.1175/JAS3599.1.

Zipser, E. J., 2003: Some views on "hot towers" after 50 years of tropical field programs and two years of TRMM data. *Cloud Systems, Hurricanes, and the Tropical Rainfall Measuring Mission (TRMM), Meteor. Monogr.*, No. 29, Amer. Meteor. Soc., 49–58.